Quarterly Report for
Contract DE-FG36-08GO18192
Stanford Geothermal Program
July-September 2011

Table of Contents

1. FRACTURE CHARACTERIZATION USING PRODUCTION DATA

This research project is being conducted by Research Assistant Egill Juliusson, Senior Research Engineer Kewen Li and Professor Roland Horne. The objective of this project is to investigate ways to characterize fractured geothermal reservoirs using production data.

1.1 SUMMARY

The focus of this report is on the development of an analytical model for thermal transport through a single fracture with a change in flow rate at a given point in time.

The report goes through the solution to the governing differential equation in detail. The reason for this is that the details were not provided by previous authors that have worked on problems similar to the one modeled here. Having a good reference to the solution process can be helpful in future research that might focus on solving slight modifications of the governing equations presented here.

The final solution to the problem is provided in two-dimensional Laplace space. Although this solution could be converted to real space, we elected to solve it using a numerical inversion code (Valkó and Abate, 2005). The result was verified by comparison to results from a discrete fracture flow simulation program. The two responses match reasonably well, and any discrepancy is likely due to numerical error.

1.2 INTRODUCTION

Our research on characterizing fractures using production data has led to a few different ways of estimating connectivity between wells in the reservoir. The focus has been on tracer, pressure and flow rate data, and in the Quarterly Reports from Winter and Spring 2011 we proposed methods for utilizing these data to optimize injection and production scheduling in fractured reservoirs.

The results so far have shown that connectivity parameters obtained from tracer, pressure and flow rate signals work reasonably well for predicting thermal breakthrough. A major unknown that is, as of yet, not included in the workflow is the effective surface area of the fracture (or equivalently, the effective fracture aperture). The surface area has a large effect on the heat transfer into the fracture, and thus the thermal breakthrough.

One way to estimate the heat transfer area is to fit an analytical model to the early stages of thermal drawdown in a production well. In that way, it might be possible to use the corrected model as a basis for reconfiguring the flow rates to reverse or dampen the rate of thermal drawdown. It would be useful, for the objective function that was used in the flow rate scheduling problem, to have an analytical expression for thermal drawdown at variable flow rates. A step towards this goal involves deriving an analytical solution for the case where the flow rate changes at a single point in time.

1.3 THERMAL TRANSPORT THROUGH A FRACTURE WITH CHANGING FLOW RATE

In this report we formulate an analytical model for thermal transport through a fracture. The fracture has aperture $2b$ and is bounded by infinitely large matrix blocks. The flow rate is assumed to have a constant value, q_1, from time $t = 0$ until $t = t_c$. After that it changes to a new rate $q_2 = q_1/\lambda$. The solution to the problem before time t_c was derived by Lauwerier (1955). The solution for $t > t_c$ is similar to the one given by Kocabas (2010), although his work focused on injection-backflow tests, whereas this model is designed for tests on injector-producer doublets. We refer to the time before the change in injection as t_1 and the time after change in injection as t_2. A schematic diagram of the problem is given in Figure 1.1. The nomenclature for the parameters displayed in the diagram is given in Table 1.1.

Thermal transport within the fracture in the x-direction occurs only by advection, not conduction. Conversely, we assume infinite thermal conductivity in the z-direction, and thus a constant temperature at any given x within the fracture. We also assume that the fracture wall has the same temperature as the fluid in the fracture and that thermal transport from the matrix to the fracture obeys Fourier's Law of conduction. Heat transport in the matrix occurs only through conduction in the z-direction.
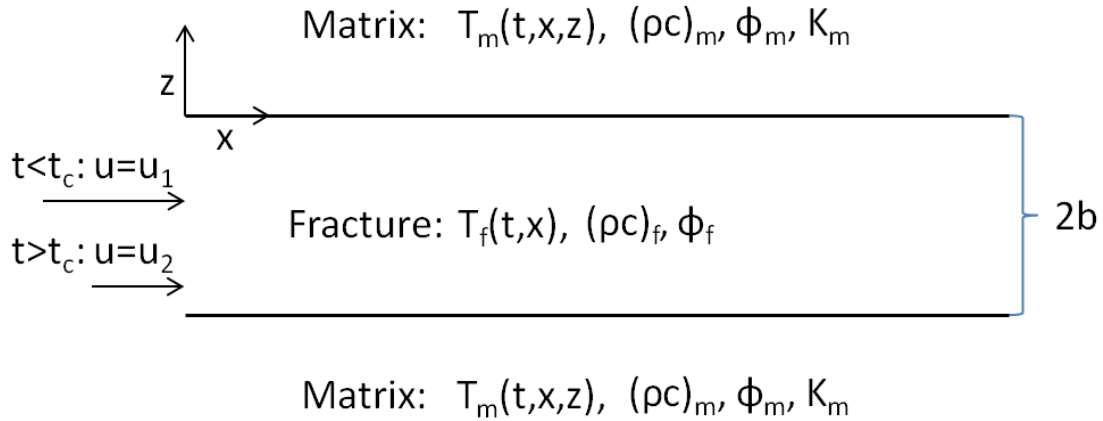

Matrix: $T_m(t,x,z)$, $(\rho c)_m$, ϕ_m, K_m

z

x

$t < t_c$: $u = u_1$

$t > t_c$: $u = u_2$

Fracture: $T_f(t,x)$, $(\rho c)_f$, ϕ_f

$2b$

Matrix: $T_m(t,x,z)$, $(\rho c)_m$, ϕ_m, K_m

Figure 1.1: Schematic diagram of the thermal transport problem through a single fracture with two flow velocities.

1.3.1 Solution before change in flow rate

The solution derived in this section is very similar to the one derived by Lauwerier in 1955. The details of how that solution is obtained are not very well recorded in the 1955 publication. Understanding that process is important to be able to derive a solution for thermal breakthrough after a change in flow rate and therefore we give the details here.

The governing equation for the variation in temperature within the fracture before the change in flow rate, i.e. before time t_c is:

$$(\rho c)_f \frac{\partial T_f}{\partial t_1} + (\rho c)_w \phi_f u_1 \frac{\partial T_f}{\partial x} - \frac{K_m}{b} \frac{\partial T_m}{\partial z}\bigg|_{z=0} = 0 \tag{0.1}$$

Similarly, the governing equation for the matrix is:

$$(\rho c)_m \frac{\partial T_m}{\partial t_1} - K_m \frac{\partial^2 T_m}{\partial z^2} = 0 \tag{0.2}$$

where the volumetric heat capacity for the fracture is:

$$(\rho c)_f = \phi_f (\rho c)_w + (1 - \phi_f)(\rho c)_r \tag{0.3}$$

and for the maxtrix:

$$(\rho c)_m = \phi_m (\rho c)_w + (1 - \phi_m)(\rho c)_r \tag{0.4}$$

All other parameters are defined in Table 1.1.

Table 1.1: Nomenclature for parameters used in the thermal transport problem

Symbol	Description
$T_f(t, x)$	Fracture temperature [C]
$T_m(t, x, z)$	Matrix temperature [C]
ρc	Volumetric heat capacity [J/m³/C]
K	Thermal conductivity [W/m/C]
q	Volumetric flow rate [m³/s]
u	Interstitial flow velocity, $u = q/(2bH\phi_f R)$, [m/s]
b	Half of fracture aperture [m]
H	Fracture height [m]
λ	Ratio between flow rates before and after t_c [-]
ϕ	Porosity [-]
R	Retardation factor, $R = 1 + \phi_m(1 - \phi_f)/\phi_f$
x	Distance in the x-direction [m]
z	Distance in the z-direction [m]
t	Time [s]
s	Laplace transform variable
Subscript	**Description**
f	Bulk property of the fracture
m	Bulk property of the matrix
w	Property of liquid water
r	Property of reservoir rock
D	Dimensionless parameter
1	Variable before time t_c
2	Variable after time t_c

Initially the fracture and matrix are all at temperature T_0

$$T_f = T_m = T_0 \qquad at \qquad t_1 = 0 \tag{0.5}$$

At the injection point we assume a constant temperature:

$$T_f = T_i \qquad at \qquad x = z = 0 \tag{0.6}$$

and the temperature infinitely far away from the fracture remains at the initial temperature:

$$T_m \rightarrow T_0 \qquad as \quad z \rightarrow \infty \tag{0.7}$$

Finally the requirement that the fracture wall must be at the same temperature as the fluid within the fracture gives the boundary condition:

$$T_f = T_m \quad at \quad z = 0 \tag{0.8}$$

To simplify further derivations we non-dimensionalize the equations as follows:

$$
\begin{aligned}
T_{fD} &= \frac{T_0 - T_f}{T_0 - T_i}, & T_{mD} &= \frac{T_0 - T_m}{T_0 - T_i}, \\
x_D &= \frac{K_m x}{(\rho c)_w \phi_f b^2 u_1}, & z_D &= \frac{z}{b}, \\
t_{1D} &= \frac{K_m t_1}{(\rho c)_f b^2}, & \theta &= \frac{(\rho c)_m}{(\rho c)_f}
\end{aligned}
\tag{0.9}
$$

This leads to the dimensionless governing equation for the fracture and matrix, respectively:

$$\frac{\partial T_{fD}}{\partial t_{1D}} + \frac{\partial T_{fD}}{\partial x_D} - \frac{\partial T_{mD}}{\partial z_D}\bigg|_{z_D=0} = 0 \tag{0.10}$$

$$\theta \frac{\partial T_{mD}}{\partial t_{1D}} - \frac{\partial^2 T_{mD}}{\partial z_D^2} = 0 \tag{0.11}$$

The initial conditions become:

$$T_{fD} = T_{mD} = 0 \quad at \quad t_{1D} = 0 \tag{0.12}$$

and the boundary conditions become:

$$T_{fD} = 1 \quad at \quad x_D = z_D = 0 \tag{0.13}$$

$$T_{mD} \to 0 \quad as \quad z_D \to \infty \tag{0.14}$$

$$T_{fD} = T_{mD} = 0 \quad at \quad z_D = 0 \tag{0.15}$$

Taking the Laplace transform with respect to time converts the Equations (0.10) and (0.11) to:

$$s_1 \bar{T}_{fD} + \frac{\partial \bar{T}_{fD}}{\partial x_D} - \frac{\partial \bar{T}_{mD}}{\partial z_D}\bigg|_{z_D=0} = 0 \tag{0.16}$$

and

$$s_1 \theta \bar{T}_{mD} - \frac{\partial^2 \bar{T}_{mD}}{\partial z_D^2} = 0 \tag{0.17}$$

The initial conditions are integrated into the governing equations but the boundary conditions become:

$$\bar{T}_{fD} = \frac{1}{s_1} \quad at \quad x_D = 0 \tag{0.18}$$

$$\bar{T}_{mD} \to 0 \quad as \quad z_D \to \infty \tag{0.19}$$

$$\bar{T}_{fD} = \bar{T}_{mD} \quad at \quad z_D = 0 \tag{0.20}$$

Equation (0.17) is a second order, linear, homogeneous ordinary differential equation which has the general solution:

$$\bar{T}_{mD} = A(s_1, x_D)e^{-\sqrt{s_1\theta}z_D} + B(s_1, x_D)e^{\sqrt{s_1\theta}z_D} \tag{0.21}$$

Boundary condition (0.19) gives $B = 0$, so $\bar{T}_{mD} = A(s_1, x_D)e^{-\sqrt{s_1\theta}z_D}$. Differentiating with respect to z_D and setting $z_D = 0$ gives:

$$\frac{\partial \bar{T}_{mD}}{\partial z_D}\bigg|_{z_D=0} = -A(s_1, x_D)\sqrt{s_1\theta} \tag{0.22}$$

Inserting this expression into Equation (0.16) yields a first-order, linear, inhomogeneous ordinary differential equation:

$$\frac{\partial \bar{T}_{fD}}{\partial x_D} + s_1 \bar{T}_{fD} = -A(s_1, x_D)\sqrt{s_1 \theta} \tag{0.23}$$

Multiplying this equation with the integrating factor $e^{s_1 x_D}$ and integrating on both sides leads to:

$$\bar{T}_{fD} = e^{-s_1 x_D} \left(\int -\sqrt{s_1 \theta} A(s_1, \tilde{x}_D) e^{s_1 \tilde{x}_D} d\tilde{x}_D + C(s_1) \right) \tag{0.24}$$

Now we use boundary condition (0.20) to obtain

$$e^{s_1 x_D} A(s_1, x_D) = \int -\sqrt{s_1 \theta} A(s_1, \tilde{x}_D) e^{s_1 \tilde{x}_D} d\tilde{x}_D + C(s_1) \tag{0.25}$$

Differentiating with respect to x_D then leads to a first order, linear, homogeneous differential equation for A:

$$\frac{\partial A}{\partial x_D} + \left(s_1 + \sqrt{s_1 \theta} \right) A = 0 \tag{0.26}$$

The general solution is:

$$A(s_1, x_D) = D(s_1) e^{-(s_1 + \sqrt{s_1 \theta}) x_D} \tag{0.27}$$

With this we can simplify Equation (0.24) to:

$$\bar{T}_{fD} = D(s_1) e^{-(s_1 + \sqrt{s_1 \theta}) x_D} + C(s_1) e^{-s_1 x_D} \tag{0.28}$$

Referring again to boundary condition (0.20) leads to:

$$D(s_1) e^{-(s_1 + \sqrt{s_1 \theta}) x_D} + C(s_1) e^{-s_1 x_D} = D(s_1) e^{-(s_1 + \sqrt{s_1 \theta}) x_D} \tag{0.29}$$

and thus $C(s_1) = 0$. Finally Equation (0.18) leads to $D(s_1) = 1/s_1$, and we have the full solution in to the problem, in Laplace space, for time $t_1 < t_c$. For the fracture it is:

$$\bar{T}_{fD}(s_1, x_D) = \frac{1}{s_1} e^{-(s_1 + \sqrt{s_1 \theta}) x_D} \tag{0.30}$$

and for the matrix:

$$\bar{T}_{mD}(s_1, x_D, z_D) = \frac{1}{s_1} e^{-(s_1 + \sqrt{s_1\theta})x_D} e^{-\sqrt{s_1\theta}z_D} \tag{0.31}$$

The inverse Laplace transform of Equations (0.30) and (0.31) can be found using the following two inversion rules:

$$L\left\{\frac{1}{s} e^{-a\sqrt{s}}\right\} = erfc\left(\frac{a}{2\sqrt{t}}\right) \quad if \quad a, t > 0 \tag{0.32}$$

$$L\{e^{-sa}\bar{F}(s)\} = F(t-a)U(t-a) \tag{0.33}$$

where $erfc$ is the complementary error function, and U is the Heaviside step function. These lead to the real space solution to the problem before the change in flow rate, which is:

$$T_{fD}(t_{1D}, x_D) = erfc\left(\frac{x_D\sqrt{\theta}}{2\sqrt{t_{1D} - x_D}}\right) U(t_{1D} - x_D) \tag{0.34}$$

for the fracture, and

$$T_{mD}(t_{1D}, x_D, z_D) = erfc\left(\frac{(x_D + z_D)\sqrt{\theta}}{2\sqrt{t_{1D} - x_D}}\right) U(t_{1D} - x_D) \tag{0.35}$$

for the matrix.

1.3.2 Solution after change in flow rate

The governing equations for the time after t_c are quite similar to the equations posed by Kocabas (2010). Kocabas was investigating thermal injection-backflow tests. This means that he was looking at the case where the flow rate is reversed, and so he had a negative sign on λ. His solution focused only on the response at $x = 0$, and that lead to a different boundary condition at that point (i.e. Equation (0.40)).

After time t_c we assume that the flow rate changes from q_1 to $q_2 = q_1/\lambda$. We call the time variable starting after the change $t_2 = t_1 - t_c$. The non-dimensionalization given in Equation (0.9) is applied again to the problem after time t_c and thus the governing equations become:

$$\frac{\partial T_{fD}}{\partial t_{2D}} + \frac{1}{\lambda}\frac{\partial T_{fD}}{\partial x_D} - \frac{\partial T_{mD}}{\partial z_D}\bigg|_{z_D=0} = 0 \tag{0.36}$$

$$\theta\frac{\partial T_{mD}}{\partial t_{2D}} - \frac{\partial^2 T_{mD}}{\partial z_D^2} = 0 \tag{0.37}$$

9

The initial conditions are now determined by the state of the fracture and matrix at time t_c. The initial conditions for the fracture are therefore:

$$T_{fD} = T_{fD}(t_{1D} = t_{cD}, x_D) \quad at \quad t_{2D} = 0 \tag{0.38}$$

Likewise, for the matrix we have:

$$T_{mD} = T_{mD}(t_{1D} = t_{cD}, x_D, z_D) \quad at \quad t_{2D} = 0 \tag{0.39}$$

The boundary conditions are:
$$T_{fD} = 1 \quad at \quad x_D = z_D = 0 \tag{0.40}$$
$$T_{mD} \to 0 \quad as \quad z_D \to \infty \tag{0.41}$$
$$T_{fD} = T_{mD} \quad at \quad z_D = 0 \tag{0.42}$$

Now taking Laplace transform with respect to t_1 yields the transformed governing equations:

$$\frac{\partial \bar{T}_{fD}}{\partial t_{2D}} + \frac{1}{\lambda}\frac{\partial \bar{T}_{fD}}{\partial x_D} - \frac{\partial \bar{T}_{mD}}{\partial z_D}\bigg|_{z_D=0} = 0 \tag{0.43}$$

$$\theta \frac{\partial \bar{T}_{mD}}{\partial t_{2D}} - \frac{\partial^2 \bar{T}_{mD}}{\partial z_D^2} = 0 \tag{0.44}$$

The initial conditions become:

$$\bar{T}_{fD} = \frac{1}{s_1} e^{-(s_1 + \sqrt{s_1\theta})x_D} \quad at \quad t_{2D} = 0 \tag{0.45}$$

and

$$\bar{T}_{mD} = \frac{1}{s_1} e^{-(s_1 + \sqrt{s_1\theta})x_D} e^{-\sqrt{s_1\theta}z_D} \quad at \quad t_{2D} = 0 \tag{0.46}$$

And the boundary conditions change to:
$$\bar{T}_{fD} = \frac{1}{s_1} \quad at \quad x_D = z_D = 0 \tag{0.47}$$

$$\bar{T}_{mD} \to 0 \quad as \quad z_D \to \infty \tag{0.48}$$
$$\bar{T}_{fD} = \bar{T}_{mD} \quad at \quad z_D = 0 \tag{0.49}$$

A second Laplace transform, now with respect to t_2 gives:

$$s_2 \bar{\bar{T}}_{fD} + \frac{1}{\lambda}\frac{\partial \bar{\bar{T}}_{fD}}{\partial x_D} - \frac{\partial \bar{\bar{T}}_{mD}}{\partial z_D}\bigg|_{z_D=0} = \frac{1}{s_1}e^{-(s_1+\sqrt{s_1\theta})x_D} \tag{0.50}$$

for the fracture. For the matrix we get:

$$s_2\theta\bar{\bar{T}}_{mD} - \frac{\partial^2 \bar{\bar{T}}_{mD}}{\partial z_D^2} = \frac{1}{s_1}e^{-(s_1+\sqrt{s_1\theta})x_D}e^{-\sqrt{s_1\theta}z_D} \tag{0.51}$$

The boundary conditions become:

$$\bar{\bar{T}}_{fD} = \frac{1}{s_1 s_2} \quad at \quad x_D = z_D = 0 \tag{0.52}$$

$$\bar{\bar{T}}_{mD} \to 0 \quad as \quad z_D \to \infty \tag{0.53}$$

$$\bar{\bar{T}}_{fD} = \bar{\bar{T}}_{mD} \quad at \quad z_D = 0 \tag{0.54}$$

Equation (0.51) is a second-order, linear, inhomogeneous ordinary differential equation. A general solution to the homogeneous equation is:

$$\bar{\bar{T}}_{mD,h} = A(s_1,s_2,x_D)e^{-\sqrt{s_2\theta}z_D} + B(s_1,s_2,x_D)e^{\sqrt{s_2\theta}z_D} \tag{0.55}$$

but we immediately see that $B = 0$ from boundary condition (0.53). A particular solution for (0.51) can be found from the method of undetermined coefficients. Thus, we guess a particular solution of the form $\bar{\bar{T}}_{mD,p} = Ke^{-\sqrt{s_1\theta}z_D}$. Inserting this particular solution into Equation (0.51) gives:

$$K = \frac{e^{-(s_1+\sqrt{s_1\theta})x_D}}{s_1\theta(s_2 - s_1)} \tag{0.56}$$

The total solution is the sum of the homogeneous and the particular solution.

$$\begin{aligned}\bar{\bar{T}}_{mD} &= A(s_1,s_2,x_D)e^{-\sqrt{s_2\theta}z_D} + \frac{e^{-(s_1+\sqrt{s_1\theta})x_D}e^{-\sqrt{s_1\theta}z_D}}{s_1\theta(s_2 - s_1)}\\ &= A(s_1,s_2,x_D)e^{-\sqrt{s_2\theta}z_D} + \frac{\bar{\bar{T}}_{fD}e^{-\sqrt{s_1\theta}z_D}}{\theta(s_2 - s_1)}\end{aligned} \tag{0.57}$$

Now apply (0.54) to get:

$$A = \bar{\bar{T}}_{fD} - \frac{\bar{\bar{T}}_{fD}}{\theta(s_2 - s_1)} \tag{0.58}$$

So for the matrix we have:

$$\bar{\bar{T}}_{mD} = \bar{\bar{T}}_{fD}e^{-\sqrt{s_2\theta}z_D} + \frac{\bar{T}_{fD}}{\theta(s_2 - s_1)}\left(e^{-\sqrt{s_1\theta}z_D} - e^{-\sqrt{s_2\theta}z_D}\right) \tag{0.59}$$

For the fracture equation (0.50) we need

$$\left.\frac{\partial\bar{\bar{T}}_{mD}}{\partial z_D}\right|_{z_D=0} = -\sqrt{s_2\theta}\bar{\bar{T}}_{fD} + \frac{\bar{T}_{fD}}{\sqrt{\theta s_1} + \sqrt{\theta s_2}} \tag{0.60}$$

Moving this expression into Equation (0.50) gives:

$$s_2\bar{\bar{T}}_{fD} + \frac{1}{\lambda}\frac{\partial\bar{\bar{T}}_{fD}}{\partial x_D} + \sqrt{s_2\theta}\bar{\bar{T}}_{fD} - \frac{\bar{T}_{fD}}{\sqrt{\theta s_1} + \sqrt{\theta s_2}} = \frac{1}{s_1}e^{-(s_1+\sqrt{s_1\theta})x_D} = \bar{T}_{fD} \tag{0.61}$$

Rearrange to get:

$$\frac{\partial\bar{\bar{T}}_{fD}}{\partial x_D} + \lambda\left(s_2 + \sqrt{s_2\theta}\right)\bar{\bar{T}}_{fD} = \lambda\left(1 + \frac{1}{\sqrt{\theta s_1} + \sqrt{\theta s_2}}\right)\bar{T}_{fD} \tag{0.62}$$

The general solution to this first order, linear, inhomogeneous ordinary differential equation is:

$$\bar{\bar{T}}_{fD} = e^{-\lambda(s_2+\sqrt{s_2\theta})x_D}\left(\int e^{\lambda(s_2+\sqrt{s_2\theta})\tilde{x}_D}\lambda\left(1 + \frac{1}{\sqrt{\theta s_1}+\sqrt{\theta s_2}}\right)\bar{T}_{fD}(s_1,\tilde{x}_D)d\tilde{x}_D + C(s_1,s_2)\right) \tag{0.63}$$

Evaluate the integral as:

$$\int e^{\lambda(s_2+\sqrt{s_2\theta})\tilde{x}_D}\lambda\left(1 + \frac{1}{\sqrt{\theta s_1} + \sqrt{\theta s_2}}\right)\bar{T}_{fD}(s_1,\tilde{x}_D)d\tilde{x}_D$$
$$= F(s_1,s_2)e^{\lambda(s_2+\sqrt{s_2\theta})x_D}e^{-(s_1+\sqrt{s_1\theta})x_D} \tag{0.64}$$

where

$$F(s_1,s_2) = \frac{\lambda}{s_1}\left(1 + \frac{1}{\sqrt{\theta s_1} + \sqrt{\theta s_2}}\right)\left(\frac{1}{\lambda(s_2 + \sqrt{s_2\theta}) - (s_1 + \sqrt{s_1\theta})}\right) \tag{0.65}$$

then Equations (0.63) and (0.64) give:

$$\bar{\bar{T}}_{fD} = F(s_1, s_2)e^{-(s_1 + \sqrt{s_1\theta})x_D} + C(s_1, s_2)e^{-\lambda(s_2 + \sqrt{s_2\theta})x_D} \tag{0.66}$$

Finally we use boundary condition (0.52) to find:

$$C(s_1, s_2) = \frac{1}{s_1 s_2} - F(s_1, s_2) \tag{0.67}$$

This gives the full solution for the temperature transient after the change in flow rate, in Laplace space. The solution for the fracture is:

$$\bar{\bar{T}}_{fD} = \frac{1}{s_1 s_2}e^{-\lambda(s_2 + \sqrt{s_2\theta})x_D} + F(s_1, s_2)\left(e^{-(s_1 + \sqrt{s_1\theta})x_D} - e^{-\lambda(s_2 + \sqrt{s_2\theta})x_D}\right) \tag{0.68}$$

and the solution for the matrix is:

$$\bar{\bar{T}}_{mD} = \bar{\bar{T}}_{fD}e^{-\sqrt{s_2\theta}z_D} + \frac{e^{-(s_1 + \sqrt{s_1\theta})x_D}}{s_1\theta(s_2 - s_1)}\left(e^{-\sqrt{s_1\theta}z_D} - e^{-\sqrt{s_2\theta}z_D}\right) \tag{0.69}$$

1.3.3 Verification and testing of the solution

The solutions given by Equations (0.68) and (0.69) were verified by making sure they satisfied Equations (0.50) and (0.51) and the boundary conditions given by Equations (0.52) through (0.54).

Expression (0.68) was inverted to real space using a number of rather tedious inversion rules. The solution had to be divided into nine different terms. Four of these terms involved a single numerical integration, and four other terms required a double numerical integration, which in some cases had nonsmooth integrands. This made the evaluation of the real space solution very inefficient and prone to error. After considerable work on computing the response this way, with limited success, we decided to abandon the real space inversion approach.

An alternative way of obtaining the real space response was to use a numerical Laplace inversion code for Equation (0.68). Valkó and Abate (2005) provide one such inversion code that is designed to invert two-dimensional functions in Laplace space. Their code is written in Mathematica and relies on some of the inner workings of that software (i.e. multiprecision computing). Inversion algorithms by Stehfest (1970) and Den Iseger (2005) were also applied, but they seemed to be poorly qualified for the inversion of this particular function.

The solution was tested by comparing predictions from the analytical model to results from a full finite element simulation using a single discrete fracture in the groundwater simulator FEFLOW. In this specific case we modeled a fracture with an aperture of 1 m, height 500 m and length 600 m. The porosity of the fracture was 0.05 and the porosity of

the matrix was 0.001. The flow rate started at 2500 m^3/day, but was reduced to 1500 m^3/day after 3000 days. The initial temperature in the reservoir was 150 C and the injection temperature was 50 C. The volumetric heat capacity for the water was 4.2e6 J/m^3/C and for the rock it was 2.5e6 J/m^3/C. The thermal conductivity of water was 0.65 W/m/C and for the rock it was 3 W/m/C. Figure 1.2 gives a snapshot of the temperature in the FEFLOW model after 10000 days.
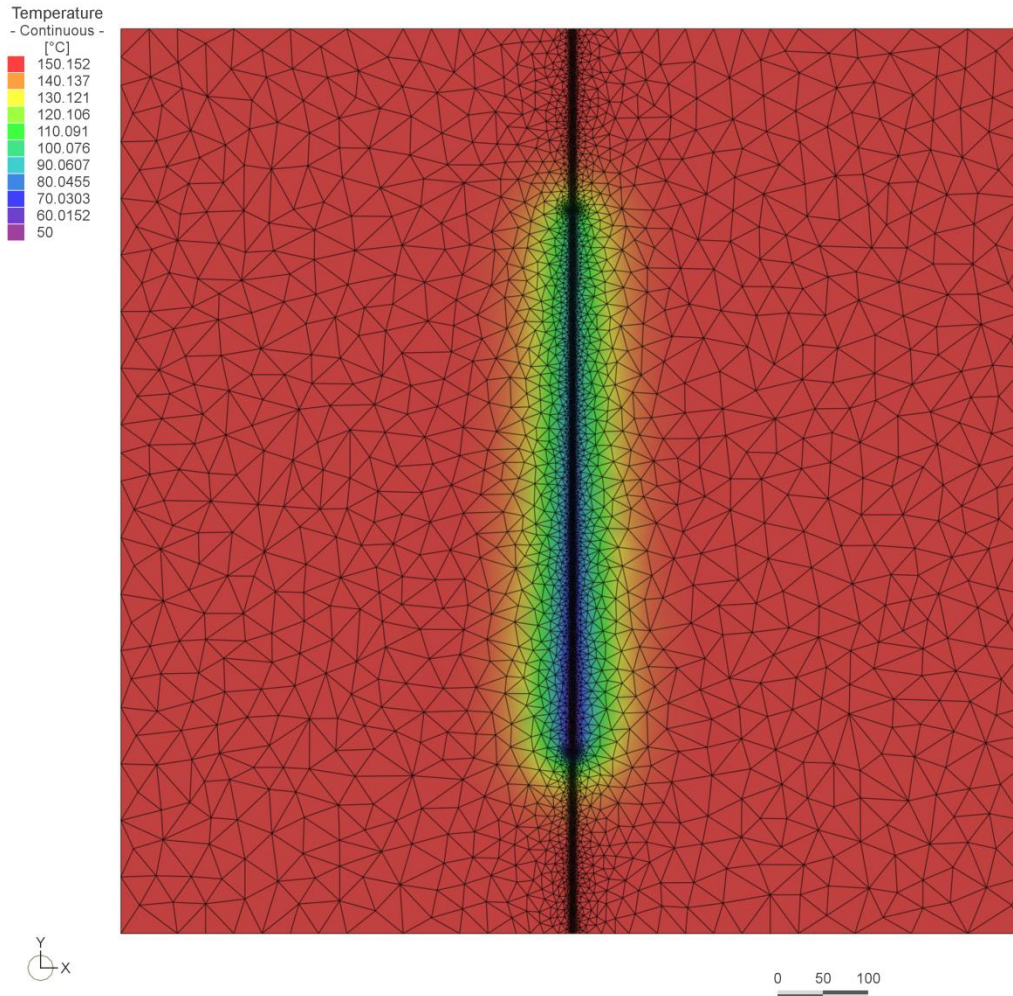

Figure 1.2: A snapshot of the fracture-matrix model created in FEFLOW, at the end of 10000 days.

A comparison of the FEFLOW computation and the analytical model results is shown in Figure 1.3. The analytical solution is quite close the results from FEFLOW although not identical. The difference may well be attributable to minor discrepancies between our theoretical model and the actual setup of the problem in FEFLOW. There may also have been numerical errors in the FEFLOW calculations and the numerical Laplace inversion.

An unfortunate drawback of the two flow rate thermal transport model is that it takes a very long time to evaluate the response after time t_c. From our experience, it takes a

slightly longer time to compute the numerical inversion of Equation (0.68) than it does to compute the response using the FEFLOW model. This would make optimizations based on this function very slow, since the optimization would require a large number of function evaluations.
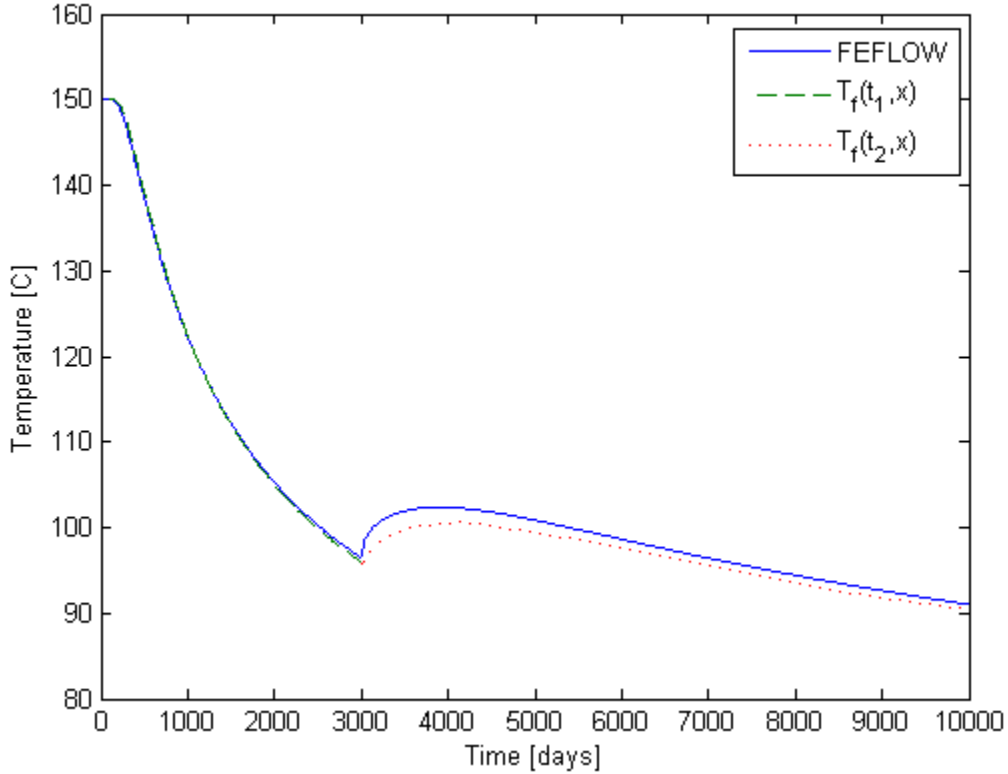

Figure 1.3: A comparison of the analytical solutions provided in this report and the simulated response to a change in flow rate, using the groundwater simulator FEFLOW. The green dashed line is computed from Equation (0.34) while the red dotted line is computed from a numerical inversion of Equation (0.68).

1.4 FUTURE WORK

The temperature transient is not the only signal we could use to infer the effective heat transfer area. It may be possible to infer the heat transfer area using either reactive tracers or thermally degrading tracers. There are some practical problems with reactive tracers because they will react with different minerals are severely different rates. This problem is avoided with thermally degrading tracers, where all one needs to estimate is the initial temperature in the system.

We will look into these types to tracers over the next quarter, and see if they could be used to refine our estimates of the effective heat transfer area. More accurate estimates of the area should lead to better predictions when solving the reinjection scheduling problem.

2. FRACTURE CHARACTERIZATION OF ENHANCED GEOTHERMAL SYSTEMS USING NANOPARTICLES

This research project is being conducted by Research Associates Mohammed Alaskar and Morgan Ames, Senior Research Engineer Kewen Li and Professor Roland Horne. The objective of this study is to develop in-situ multifunction nanosensors for the characterization of Enhanced Geothermal Systems (EGS).

2.1 SUMMARY

During this quarter, we began investigation of microparticle flow in a glass fracture model. The experimental apparatus and standard measurements of fracture hydraulic aperture and permeability were completed. The fracture aperture was found to be around 57 µm, with corresponding average permeability of 272 darcy.

Silica microspheres were injected into the glass fracture model, and it was found that 2 µm microspheres of could be transported through the fracture, with a cumulative recovery of about 76%. This injection serves as a baseline experiment for future injections using the glass fracture model.

2.2 INTRODUCTION

Last quarter (April–June, 2011), a naturally fractured greywacke core from The Geysers was prepared for the injection of fluorescent silica microspheres. The silica microspheres of different sizes were injected into the naturally fractured greywacke core sample. The effluent samples were analyzed using optical microscopy and fluorescence spectrometry. The fluorescence intensity was related to effluent concentration by constructing a calibration curve. The return curve was then estimated. We also demonstrated the potential of using microparticles and/or nanoparticles to estimate the fracture aperture by relating the physical size of the largest recovered particle to the aperture of the fracture (i.e. a fracture caliper concept).

During this quarter, we further investigated the fracture caliper concept by injecting silica microspheres into glass fracture model. The glass fracture model was prepared for the injection of silica microspheres. The preparation of the fracture model included the estimation of the hydraulic aperture and permeability of the fracture. A baseline injection was also conducted. Effluent samples were characterized using fluorescence spectrometry.

2.3 GLASS FRACTURE MODEL

Last quarter, a preliminary investigation of the flow mechanism of nanoparticles was conducted by injecting fluorescent silica microspheres through a naturally fractured greywacke core. We demonstrated the possibility of using microspheres to estimate fracture aperture (fracture caliper) by injecting a polydisperse microsphere sample into a fracture with a predetermined hydraulic aperture. We used the glass fracture model to further investigate the fracture caliper concept.

2.3.1 Fracture model description

The fracture apparatus used was designed originally to study the multiphase flow of gas and liquid phases through fractures. The apparatus was designed and fabricated by a previous researcher Gracel Diomampo in the Stanford Geothermal Program (Gracel Diomampo, MS Thesis, 2001).

The fracture model consists of a smooth glass plate placed on top of an aluminum flat surface. The seal was achieved by placing an o-ring (Viton 1/8" thick #2-272) between the glass (top) and aluminum (bottom) plates. A metal frame was bolted to the bottom plate to improve the seal. The metal frame was designed with supporting beams to prevent glass deformation due to system pressure. The spacing between these two surfaces is the simulated fracture of predetermined width and length (4 by 12 inches). The fracture model is pictured in Figure 2.1.
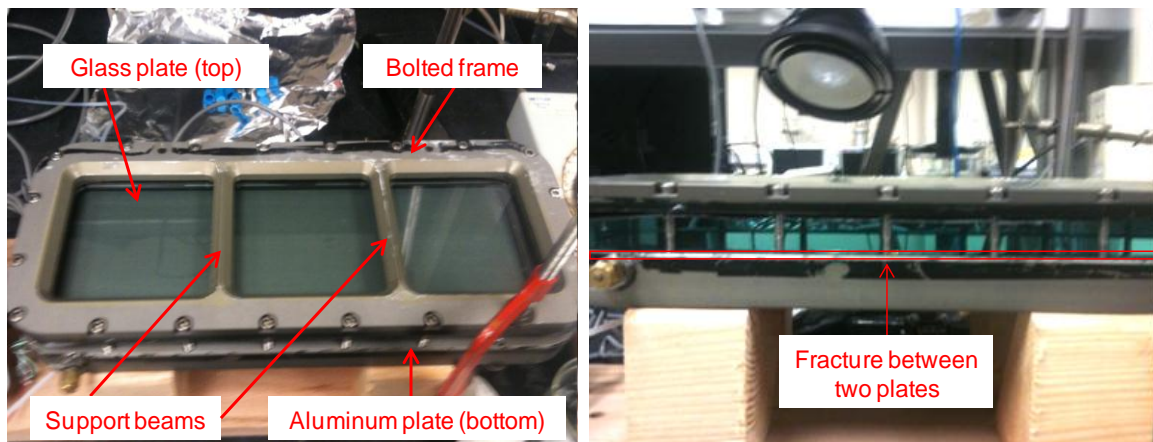

Figure 2.1: Picture of glass fracture apparatus. It shows the bolted frame, top and bottom plates and fracture location.

As the fracture apparatus was designed originally to study two-phase flow, each fluid enters the fracture through two separate inlet ports, a total of 123 capillary ports, each 0.51 mm in diameter. These ports were aligned to the fracture surface alternately. Four pressure ports with a diameter of 0.51 mm were drilled at locations throughout the fracture area. Temperature ports were also drilled, but not used during the particle injection experiments. The fluids exit the fracture through a single outlet. A schematic diagram of the fracture apparatus is shown in Figure 2.2.
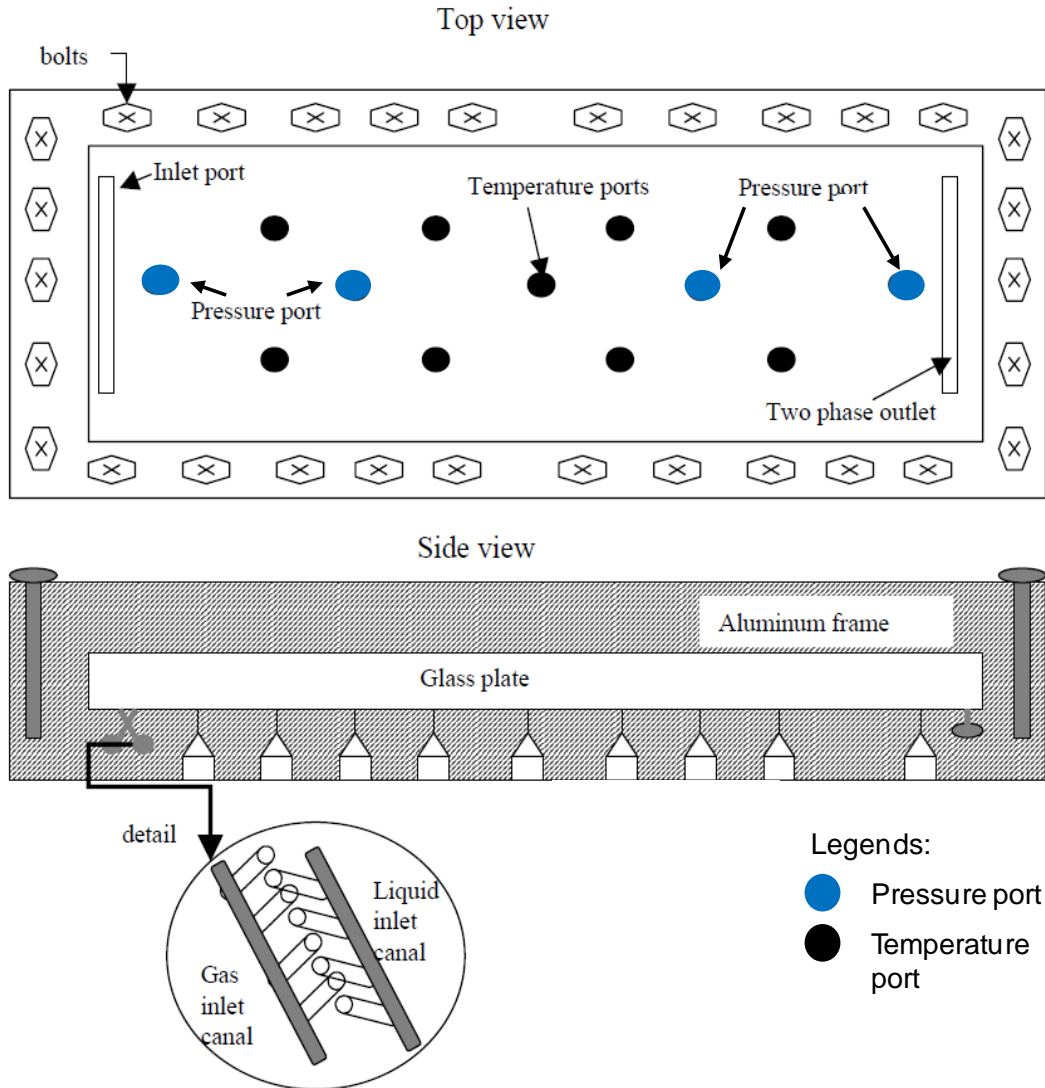
Figure 2.2: Schematic of the fracture apparatus (adapted from Diomampo, 2001).

2.3.2 Pressure and flow rate measurements

The pressure difference through the fracture was obtained using low capacity differential transducers. Two liquid-filled differential transducers (Validyne Transducer, model DP-215, range 0-1.5 psi and 0-5 psi) were attached to inlet and outlet pressure ports. Both differential pressure transducers were calibrated using a standard pressure gauge with an accuracy of 0.1 psi. The pressure transducer calibration curves are depicted in Figures 2.3 and 2.4. The pressure calibration curves indicate a good agreement between the standard pressure gauge and the differential pressure transducers.
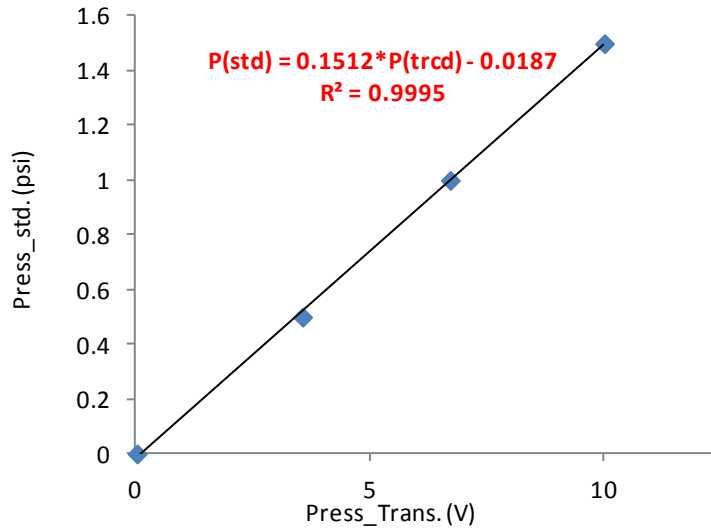
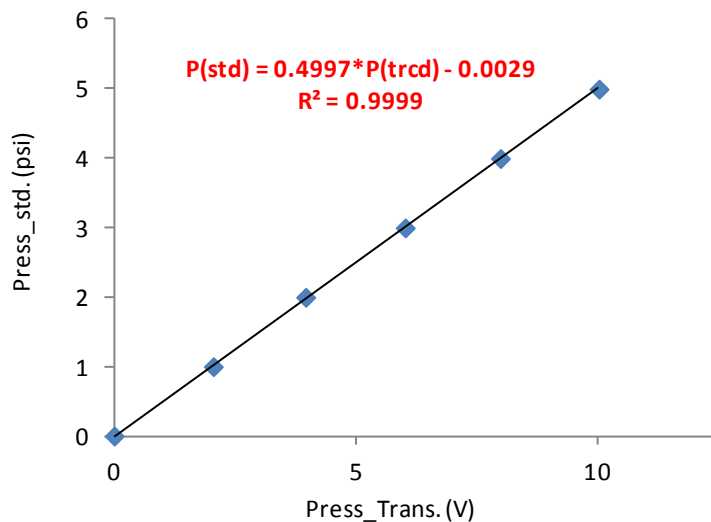*Figure 2.3: Calibration curve of the inlet pressure transducer.*

Figure 2.4: Calibration curve of the outlet pressure transducer.

A water pump (Dynamax, Model SD-200) manufactured by RAININ Instrument Company was used to inject the deionized water. The minimum pumping rate of the pump is 0.2 ml/min with an accuracy of 0.01 ml/min. This pump is an automated constant-rate pump. The flow rates of the water pump were calibrated before the experiment using a stop-watch and a Mettler balance (Model PE 300). The accuracy of the balance is 0.01 g and the range is from 0 to 300 g. The calibration curve for this pump at room temperature is shown in Figure 2.5. The measured flow rates were consistent with those specified on the pump.
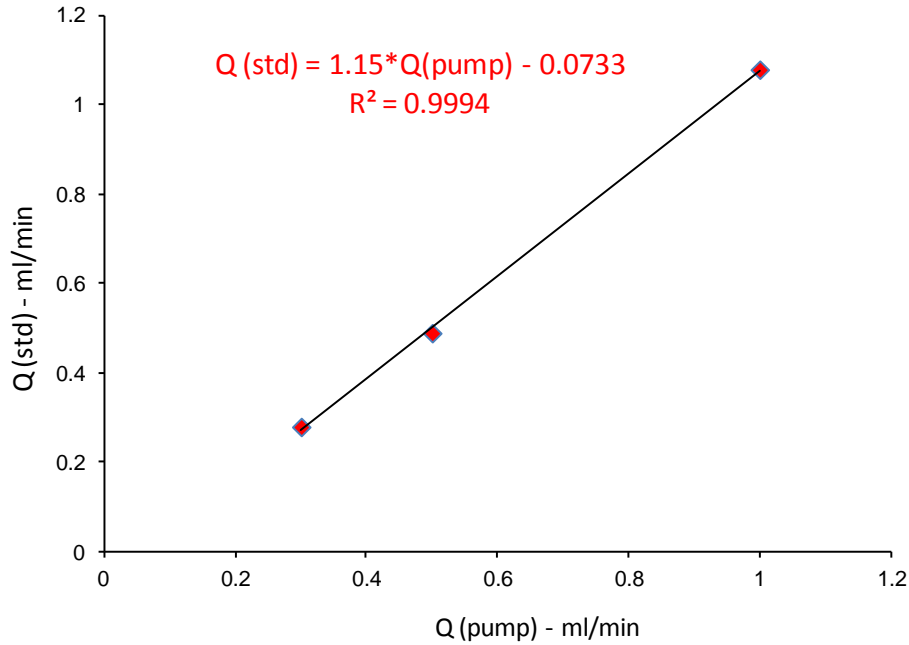
Figure 2.5: Water pump calibration curve.

2.3.3 Fracture hydraulic aperture and permeability measurements

Prior to permeability or hydraulic aperture measurements, the fracture was saturated with the testing fluid (i.e. deionized water). Air removal via vacuum and resaturation with water was not possible because the system was not designed to withstand vacuum. Instead, the saturation was achieved by first saturating the system with CO_2 then deionized water, as CO_2 dissolves more easily in water than air. The fracture apparatus was also tilted by 45 degrees for gravity to aid the saturation process.

The determination of the fracture hydraulic aperture was necessary to test the fracture caliper concept. The hydraulic aperture of the fracture was determined using the cubic law. The cubic law is given as:

$$Q = \frac{b^3}{12} \frac{bD\Delta p}{\mu L} \tag{2.1}$$

$$k = \frac{b^2}{12} \tag{2.2}$$

where Q is the flow rate in cubic meters per second, b is the fracture aperture in meter, D is the fracture width in meter, Δp is the pressure drop across the core sample in Pascal, L is the length of the fracture in meter, μ is the test fluid viscosity in Pascal second and k is the permeability in square meters. The permeability can be expressed in Darcy units using the following conversion:

$$1 darcy = 9.869 \times 10^{-13} m^2 \tag{2.3}$$

21

The aperture of the fracture was set by installing spacers made from stainless steel shims with specific thicknesses. Initially, shims with thickness of 51 μm and 102 μm were used. For both cases, the hydraulic aperture measurements were found to be around 185 μm, indicating that the aperture measurements were insensitive to shims size of 102 μm or smaller. For example, fracture aperture and permeability measurements with the shims installed can be seen in Figure 2.6.
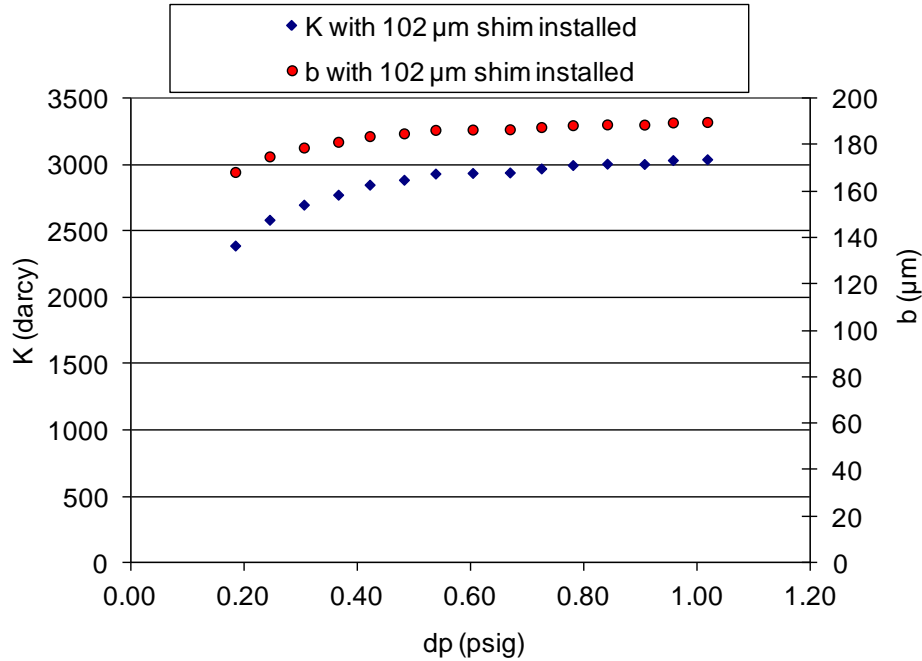

Figure 2.6: Aperture and permeability measurements as function of fracture pressure when 102 μm shims installed.

It was observed that the absolute permeability was changing with flow rate for fracture pressures below about 0.5 psig. This implied that the fluid was lifting the glass as it flowed through the fracture. At pressures greater than 0.5 psi, the glass was lifted to its maximum height contrained by the confinement of the metal frame. At this pressure range, the absolute permeability was constant and found to be around 3100 darcy. To confirm the validity of Darcy's law (i.e. flow in fracture is laminar and that inertia effect is negligible), we examined the linearity between single-phase pressure drop and flow rate. Figure 2.7 shows a linear relationship between the pressure drop and flow rate, indicating the negligible effect of inertia on the flow within the fracture.
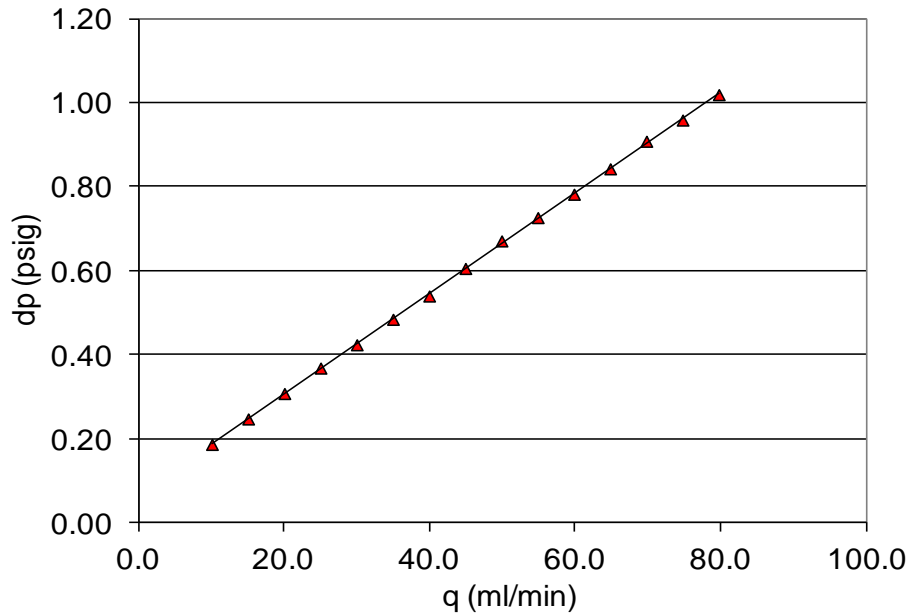
Figure 2.7: Steady-state, single-phase pressure drop versus flow rates during aperture measurements with 102 µm shims installed. Linearity between pressure drop and flow rate confirmed, hence, Darcy's law holds.

Due to the inconsistency between the measured fracture hydraulic aperture (185 µm) and shim size (102 µm), further investigation was carried out. The hydraulic aperture was measured after the removal of the shims. In this case, only the o-ring exists between the glass and aluminum plates. The hydraulic aperture of the fracture was found to be around 57 µm with an average permeability of 272 darcy. This implied that the o-ring was compressed to a minimum height of about 57 µm. When shims were installed, the additional thickness of shims was added. If fracture surfaces were perfectly flat, the measured fracture aperture should be the sum of the o-ring and shim thicknesses (i.e. 102 µm plus 57 µm or total of 159 µm). The difference between measured aperture and expected value (about 26 µm) was believed to be a result of irregularities of the flat surfaces. The fracture aperture and permeability measurements without shims can be seen in Figures 2.8. To avoid uncertainty of aperture measurements, it was decided to use the model without shims during injection of microparticles. Hence we designed the influent sample to have particles smaller and bigger than 57 µm.
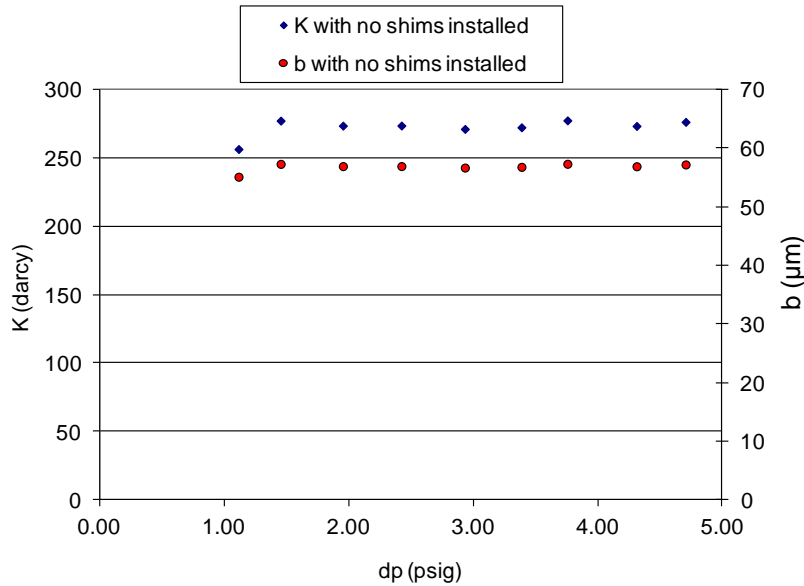
Figure 2.8: Aperture and permeability measurements as function of fracture pressure when 102 µm shims installed.

2.4 FLUORESCENT SILICA MICROSPHERES INJECTION EXPERIMENT: GLASS FRACTURE MODEL

The objectives of this experiment were to investigate the transport and recovery of fluorescent silica microspheres through the glass fracture model, to study the relationship between the size of recovered microparticles and fracture aperture. Several injections were conducted with silica microspheres through a fractured greywacke core. We intended to explore the possibility of measuring the fracture aperture further by using the size of the largest recovered particles. As a baseline experiment, we injected silica microspheres (2 µm) of the size about 4% of the fracture aperture. The goal was to verify that the silica microspheres were not trapped within the fracture due to chemical or electrostatic forces. The next step will be to inject a polydisperse sample with microparticles bigger and smaller than fracture aperture.

This section provides the silica microsphere injection experiment details. The characterization of the blue fluorescent silica microspheres can be found in the previous quarterly report (April-June, 2011).

2.4.1 Experimental method used in the glass fracture model injections

The fluorescent silica microspheres injection was conducted to investigate their flow through the glass fracture model. The testing apparatus was similar to the hydraulic aperture and permeability measurements experiment, but modified slightly to allow for the injection of microparticles. The configuration also allows for injection of particle-free deionized water, without interrupting the flow. The modified apparatus can be seen in Figure 2.9.
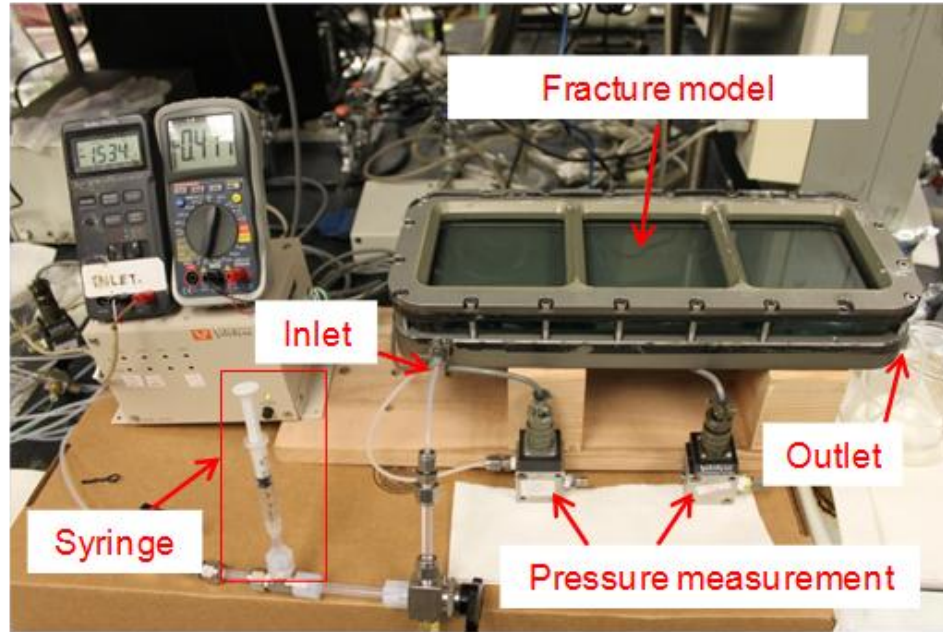
Figure 2.9: A picture of the fluorescent silica microsphere injection apparatus.

The nanofluid was contained in a syringe downstream the water pump. The microparticles were injected using the syringe. The silica microspheres sample of original concentration of 4.99×10^{-2} *g/cm³* was diluted by a factor of 100 using deionized water. The new concentration of injected silica microsphere influent was 4.99×10^{-4} *g/cm³*. Prior to the injection of the microfluid, the fracture model was preflushed with several pore volumes of water. Following the injection of the microparticles (1 *cm³*), a continuous flow of water was introduced. Effluent samples were then collected, and fluorescence spectrometry was used to determine the concentration of the silica microspheres in effluent samples.

2.5 RESULTS

The fluorescent silica microspheres were transported through the fracture model successfully.

The recovery of the silica microspheres was estimated by measuring the emission spectra and correlating it to the effluent concentration using a calibration curve. The fluorescence emission spectra of all effluent samples collected during the blue silica microsphere injection are shown in Figure 2.10. The samples were excited at a wavelength of 350 *nm* and the emission spectra were measured between 350 to 600 *nm*, with a peak or maximum emission at a wavelength of about 430 *nm*. Note that the emission peaks of samples B3 and B4 were not shown clearly because of the low content of silica particles, compared to the concentration of sample B2 that contains the bulk of the silica microspheres. Despite the fact that the effluent samples volume was 0.5 ml, this is significantly higher than the pore volume of the fracture and therefore the majority of particles were captured in one sample (B2). To construct the calibration curve, the emission spectra of a few samples of known

concentrations were acquired. The concentrations of effluent samples were determined based on the maximum emission intensity at the peak (Figure 2.11).
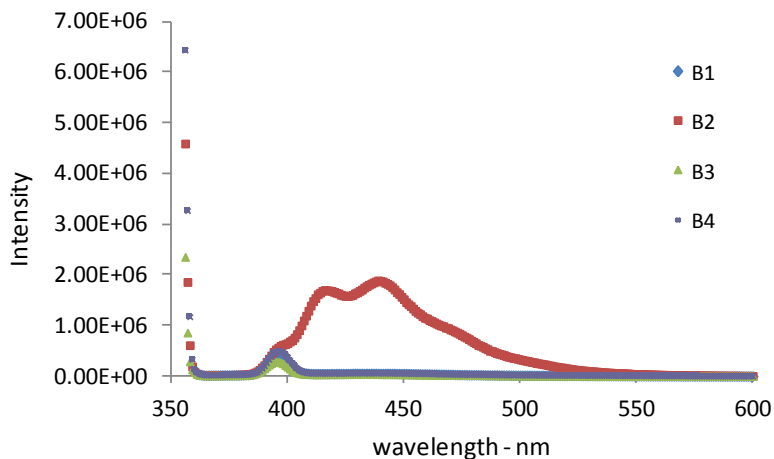

Figure 2.10: Emission spectra of effluent samples during injection of the blue silica spheres.
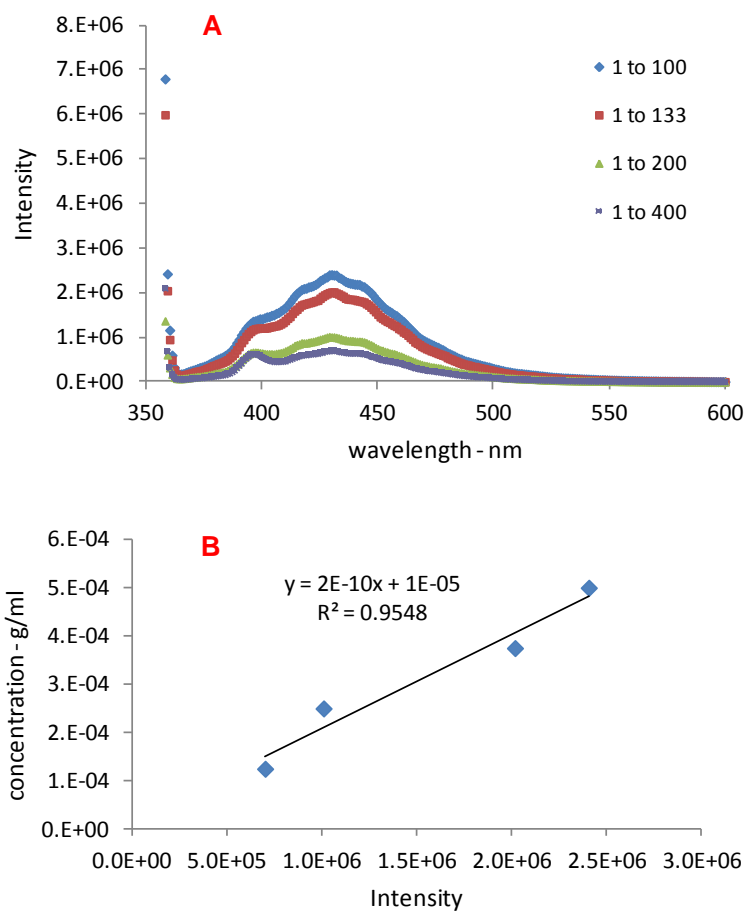

Figure 2.11: (A) Emission spectra of diluted silica samples of known concentrations, (B) calibration curve.

26

The return curves of the blue microspheres were then estimated as shown in Figure 2.12. It was found that cumulative recovery of injected blue silica microspheres was about 70%. Estimation of the cumulative recovery of the silica spheres was also attempted by calculating the cumulative ratio of emission intensity of effluent (I) to emission intensity of influent (I_o). Based on the intensity ratio, the cumulative recovery was about 76%. Both recovery values were reasonably in agreement. The slight difference may be attributed to error introduced during the construction of the calibration curve. The unrecovered silica microspheres were believed to be trapped within fittings and/or valves used for their injection.
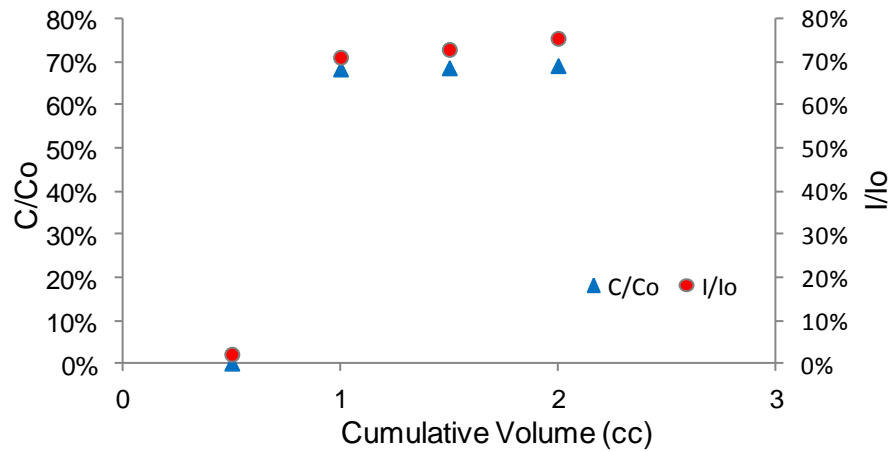
Figure 2.12: Cumulative recovery of silica microspheres calculated based on concentration and intensity ratios.

2.6 FUTURE WORK

We will continue our investigation of the flow of particles through the glass fracture model. We plan to inject a polydisperse sample with particles bigger and smaller than predetermined hydraulic aperture, to further investigate the fracture caliper concept. As the model allows for visual study of particle flow, we also plan to investigate the diffusion of particles visually during flow.

3. FRACTURE CHARACTERIZATION USING RESISTIVITY

This research project is being conducted by Research Assistant Lilja Magnusdottir, Senior Research Engineer Kewen Li and Professor Roland Horne. The objective of this project is to investigate ways to use resistivity to infer fracture properties in geothermal reservoirs.

3.1 SUMMARY

In this project, the aim is to use Electrical Resistivity Tomography (ERT) to characterize fracture properties in geothermal fields. The resistivity distribution of a field can be estimated by measuring potential differences between various points while injecting an electric current into the ground and resistivity data can be used to infer fracture properties due to the large contrast in resistivity between water and rock. The contrast between rock and fractures can be increased further by injecting a conductive tracer into the reservoir, thereby decreasing the resistivity of the fractures. In this project, the potential difference has been calculated between two points (an injector and a producer) as conductive fluid flows through fracture networks. The time history of the potential field depends on the fracture network and can therefore be used to estimate where fractures are located and the character of their distribution.

The analogy between Ohm's law that describes electrical flow and Darcy's law describing fluid flow makes it possible to use flow simulator TOUGH2 to calculate electric fields. This report illustrates how EOS1 module in TOUGH2 has previously been used to calculate the potential field as conductive fluid is injected into the reservoir and discusses how EOS9 module in TOUGH2 can be used instead of EOS1 to get accurate results of the electric field. In EOS9 the density and viscosity can be defined as constants instead of being pressure dependent, allowing for a simulation of an electric field without the resistivity becoming dependent on the electric potential. A few simple simulations were performed and results compared to the resistivity model previously described in the January-March 2011 quarterly report. The advantage of using TOUGH2 to solve the electrical field instead of the resistivity model is that the same grid can be used for both electric and fluid flow models. TOUGH2 also allows use of nonrectangular elements making the simulation faster and more efficient.

Future work includes studying further the relationship between fracture networks and the change in potential differences as conductive tracer is injected into the reservoir for more complicated fractal network of fractures. It also includes implementing self-potential calculations into the model since the change in self-potential affects the measured potential difference and could facilitate fracture characterization. Another future goal is to study the possibility of using the potential differences with inverse modeling to characterize fracture patterns as well as to study different electrode layouts. It is also of interest to explore the use of nanotracers and the influence of injecting varying tracer concentrations.

3.2 INTRODUCTION

Characterizing the dimensions and topology of fractures in geothermal reservoirs is crucial for optimal designing of production and to find feasible drilling locations. Fractures carry most of the fluid in the reservoir so fracture configuration is central to the performance of a

geothermal system both in fractured reservoirs as well as in Enhanced Geothermal System (EGS) applications. The knowledge of fluid-flow patterns is necessary to ensure adequate supply of geothermal fluids and efficient operation of geothermal wells and to prevent short-circuiting flow paths from injector to producer that would lead to premature thermal breakthrough. Fracture characterization therefore increases the reliability of geothermal wells and the overall productivity of geothermal power plants.

The goal of this study is to find ways to use Electrical Resistivity Tomography (ERT) to characterize fractures in geothermal reservoirs. ERT is a technique for imaging the resistivity of a subsurface from electrical measurements. Pritchett (2004) concluded based on a theoretical study that hidden geothermal resources can be explored by electrical resistivity surveys because geothermal reservoirs are usually characterized by substantially reduced electrical resistivity relative to their surroundings. Electrical current moving through the reservoir passes mainly through fluid-filled fractures and pore spaces because the rock itself is normally a good insulator. In these surveys, a direct current is sent into the ground through electrodes and the voltage differences between them are recorded. The input current and measured voltage difference give information about the subsurface resistivity, which can then be used to infer fracture locations.

Resistivity measurements have been used in the medical industry to image the internal conductivity of the human body, for example to monitor epilepsy, strokes and lung functions as discussed by Holder (2004). In Iceland, ERT methods have been used to map geothermal reservoirs. Arnarson (2001) describes how different resistivity measurements have been used effectively to locate high temperature fields by using electrodes located on the ground's surface. Stacey et al. (2006) investigated the feasibility of using resistivity to measure saturation in a rock core. A direct current pulse was applied through electrodes attached in rings around a sandstone core and it resulted in data that could be used to infer the resistivity distribution and thereby the saturation distribution in the core. It was also concluded by Wang and Horne (2000) that resistivity data have high resolution power in the depth direction and are capable of sensing the areal heterogeneity.

In the approach considered in this project so far, electrodes would be placed inside two geothermal wells and the potential differences between them studied to locate fractures and infer their properties. Due to the limited number of measurement points, the study is investigating ways to enhance the process of characterizing fractures from sparse resistivity data. For example, in order to enhance the contrast in resistivity between the rock and fracture zones, a conductive tracer would be injected into the reservoir and the time-dependent voltage difference measured as the tracer distributes through the fracture network.

Slater et al. (2000) have shown a possible way of using ERT with a tracer injection by observing tracer migration through a sand/clay sequence in an experimental $10 \times 10 \times 3$ m^3 tank with cross-borehole electrical imaging. Singha and Gorelick (2005) also used cross-well electrical imaging to monitor migration of a saline tracer in a $10 \times 14 \times 35$ m^3 tank. In previous work, usually many electrodes were used to obtain the resistivity distribution for

the whole field at each time step. The resistivity distribution was then compared to the background distribution (without any tracer) to see resistivity changes in each block visually, to locate the saline tracer and thereby the fractures. Using this method for a whole reservoir would require a gigantic parameter space, and the inverse problem would not likely be solvable, except at very low resolution. However, in the method considered in this study, the potential difference between the wells would be measured and plotted as a function of time while the conductive tracer flows through the fracture network. Future work will involve using that response, i.e. potential difference vs. time, in an inverse modeling process to characterize the fracture pattern.

First, the analogy between water flow and electrical flow is defined and the possibility of using TOUGH2 flow simulator to solve an electric field is investigated. Next, electric field time histories calculated using EOS1 module in TOUGH2 for three different fracture networks are illustrated. The possibility of using EOS9 module instead of EOS1 to get accurate results for the electric potential is investigated by calculating the electric field for three simple cases and comparing the analytical solution to the results from EOS9, EOS1 and the resistivity model previously described in the January-March 2011 quarterly report. Finally, future work is outlined.

3.3 WATER FLOW ANALOGY OF ELECTRICAL FLOW

The steady-state flow of an electric current through a conducting medium due to differences in energy potential is analogous to the steady-state flow of a fluid through porous medium. Darcy's law is an empirical relationship similar to Ohm's law,

$$J = -\sigma \nabla \phi \tag{3.1}$$

where J is current density [A/m^2], σ is the conductivity of the medium [Ωm] and ϕ is the electric potential [V] but instead of describing electrical flow Darcy's law describes fluid flow through a porous medium,

$$q = -\frac{k}{\mu} \nabla p \tag{3.2}$$

where q is the flow rate [m/s], k is permeability [m^2], μ is viscosity of the fluid [kg/ms] and p is pressure [Pa]. Table 3.1 presents the correspondence between the variables and relations of water flow (Darcy's law) and electric current flow (Ohm's law).

Table 3.1: Correspondence between electric current flow and water flow.

	Darcy's law: $q = -\dfrac{k}{\mu} \nabla p$	Ohm's law: $J = -\sigma \nabla \phi$
Flux of:	Water q [m/s]	Charge J [A/m^3]
Potential:	Pressure p [Pa]	Voltage ϕ [V]
Medium property:	Hydraulic conductivity $\dfrac{k}{\mu}$ [m^2/Pa·s]	Electrical conductivity σ [1/Ωm]

The similarities between these two equations imply that it is possible to use flow simulator like TOUGH2 to solve electric field due to flow of electric current. Then, the pressure results from TOUGH2 would correspond to the electric voltage, the current density to the flow of water and the electrical conductivity would correspond to the hydraulic conductivity, i.e.

$$\sigma = \frac{k}{\mu} \tag{3.3}$$

However, it must be taken into account that viscosity depends on pressure while conductivity of a reservoir does not depend on the electric voltage used. Figure 3.1 shows how viscosity of water at 150°C changes with pressure.
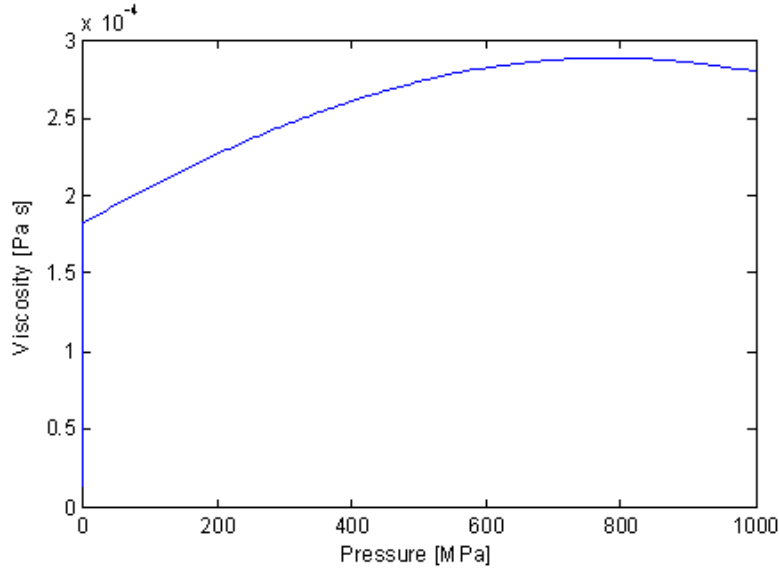

Figure 3.1:   Viscosity [Pa·s] as a function of pressure [MPa].

In order to take the pressure dependence into account EOS9 module in TOUGH2 was studied. EOS9 considers flow of a single aqueous phase consisting of a single water component. The conditions are assumed to be isothermal so only a single water mass balance equation is solved for each grid block and the thermal properties of water can be overwritten. Therefore, liquid viscosity, density and compressibility can be defined constant and reference pressure and temperature can be overwritten, making the imitation of electric flow possible.

In TOUGH2, Darcy's law is solved using the following discretization,

$$F_{nm} = \rho u_{nm} = -k_{nm} \left[\frac{k_r \rho}{\mu} \right]_{nm} \left[\frac{P_n - P_m}{D_{nm}} - \rho_{nm} g_{nm} \right] \tag{3.4}$$

where ρ is density and g_{nm} is gravity in direction from m to n. Suitable averaging are used at the interface between grid blocks n and m, and D_{nm} is the distance between the nodal points n and m (see Figure 3.2).
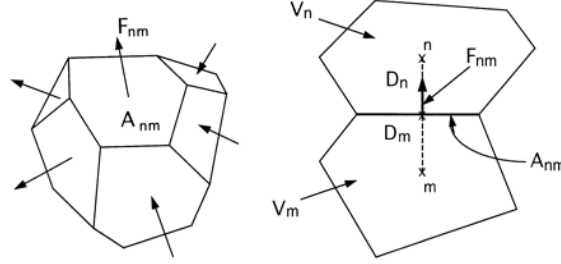
Figure 3.2: Space discretization, grid blocks n and m.

In order to calculate the flow simulation the following equation is solved using Newton/Raphson iteration:

$$R_n^{K,K+1} = M_n^{K,K+1} - M_n^{K,K} - \frac{\Delta t}{V_n}\left[\sum_m A_{nm}F_{nm}^{K,K+1} + V_n q_n^{K,K+1}\right] \tag{3.5}$$

where $R_n^{K,K+1}$ are residuals between time step t^k and $t^{k+1} = t^k + \Delta t$, M is mass accumulation, A is the surface area of the grid block, V is the volume and q denotes sinks and sources.

The pressure solved in a flow simulation is of higher magnitude than the voltage in the electric case would ever be, so some of the electric parameters need to be scaled in order to solve the electric problem using a flow simulator. Table 3.2 shows the scaling of the electrical parameters for the flow simulation where the density of the fluid has been taken into account as well.

Table 3.2: Scaling of electric parameters.

Electric parameters:	Multiplied by:	Flow parameters:
ϕ [V]	10^6	P [Pa]
J [A/m^3]	10^9	q [m/s]
D [m]	10^6	D [m]
A [m^2]	10^{12}	A [m^2]
V [m^3]	10^{12}	V [m^3]

The initial pressure is set to 10^6 Pa so in order to get the electric potential results assuming initial voltage to be zero, the initial pressure is subtracted from the pressure results and the results are then multiplied by 10^{-6} to get the electric voltage results.

3.4 RESULTS

Previously, a flow simulation was performed using EOS1 module in TOUGH2 reservoir simulator to see how a tracer, which increases the conductivity of the fluid, distributes after being injected into the reservoir. The simulation was carried out on a two-dimensional grid with dimensions $1000 \times 1000 \times 10$ m^3 with fractures first modeled as a cross in the upper left corner (green blocks) as shown in Figure 3.3, then as a larger cross in the upper left corner as Figure 3.4 shows and finally with no fractures.
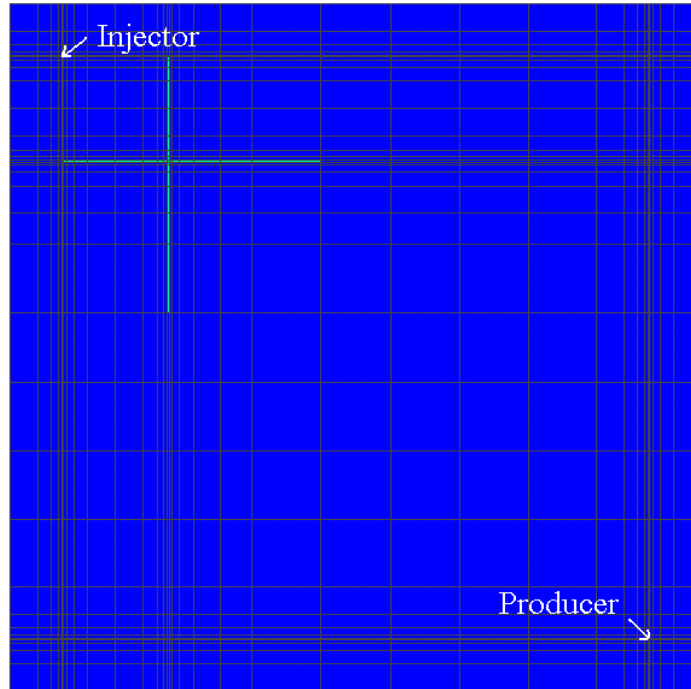
Figure 3.3: Fractures (green blocks) modeled as a small cross in the upper left corner of the reservoir.

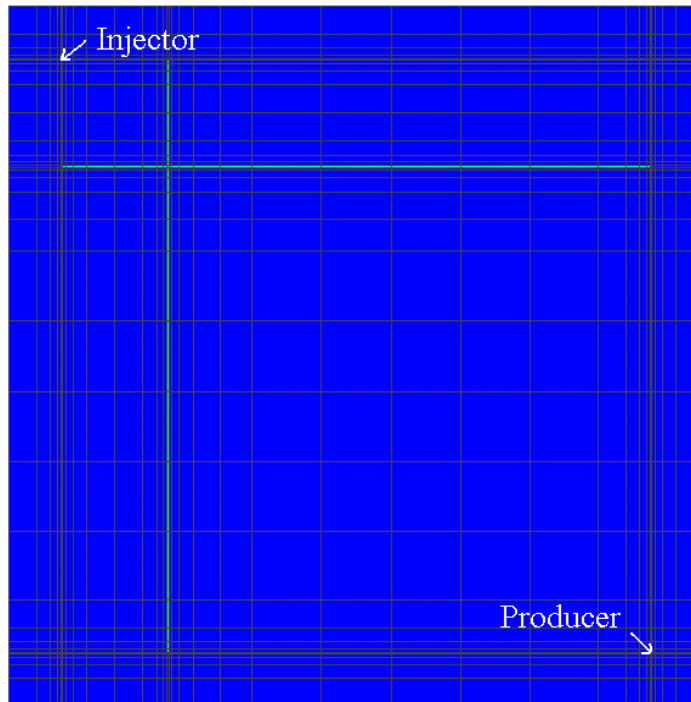*Figure 3.4: Fractures (green blocks) modeled as a larger cross in the upper left corner of the reservoir.*

The goal was to study the difference in potential field between these three cases as conductive fluid is injected into the reservoir. The reservoir is modeled with porosity 0.2 and permeability 10^5 md (10^{-10} m^2) while the fractures have permeability 5×10^9 md ($5 \times$

10^{-4} m^2). No-flow boundary conditions were used and 100 kg/s of water was injected in the upper left corner with enthalpy 100 kJ/kg, and 0.1 kg/s of tracer with enthalpy 100 kJ/kg. The initial pressure was set to 10 atm, temperature to 150°C and initial tracer mass fraction to 10^{-9} because the simulator could not solve the problem with zero initial tracer mass fraction.

The tracer injected into the reservoir is a NaCl solution which resistivity changes with temperature and concentration. Ucok et al. (1980) have established experimentally the resistivity of saline fluids over the temperature range 20-350°C and their results for resistivity of NaCl solution calculated using a three-dimensional regression formula is shown in Figure 3.5.
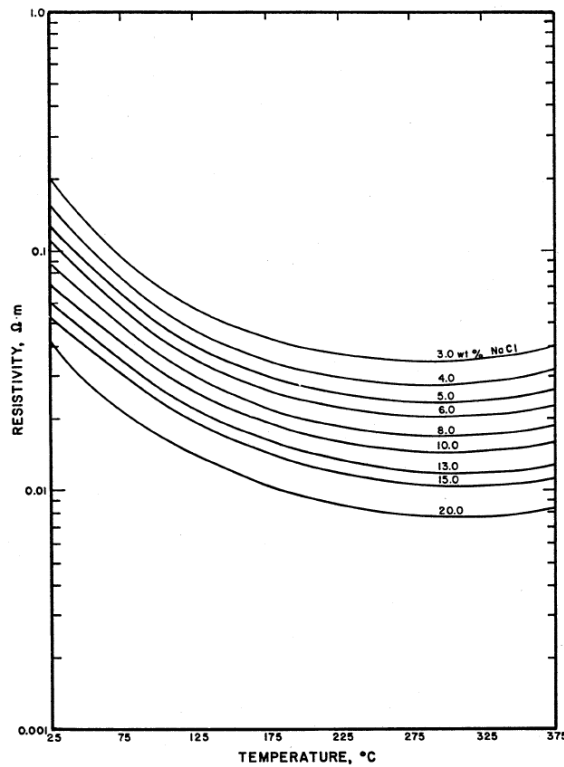

Figure 3.5: Resistivity of NaCl solution as a function of temperature and concentration (Ucok et al., 1980).

Ucok et al. calculated that the dependence of resistivity is best represented by the formula:

$$\rho_w = b_0 + b_1 T^{-1} + b_2 T + b_3 T^2 + b_4 T^3 \tag{3.6}$$

where T is temperature and b are coefficients found empirically. The best fit for the concentration dependence was found to be:

$$\rho_w = 10/(\Lambda c) \tag{3.7}$$

where:

$$\Lambda = B_0 - B_1 c^{1/2} + B_2 c \ln c + higher\ order\ terms \tag{3.8}$$

Coefficients B depend on the solution chemistry and c is the molar concentration.

In this project, the tracer concentration resulting from the flow simulation is changed into molar concentration and the following *B* coefficient matrix for the three-dimensional regression analysis of the data studied by Ucok et al. (1980) is used to calculate the resistivity of the NaCl solution,

$$B = \begin{array}{ccc} 3.470 & -6.650 & 2.633 \\ -59.23 & 198.1 & -64.80 \\ 0.4551 & -0.2058 & 0.005799 \\ -0.346E\text{-}5 & 7.368E\text{-}5 & 6.741E\text{-}5 \\ -1.766E\text{-}6 & 8.787E\text{-}7 & -2.136E\text{-}7 \end{array}$$

Therefore, the resistivity value of each block depends on the tracer concentration in that block and the value decreases as more tracer flows into the block.

The EOS1 module in TOUGH2 was used to calculate the electric potential distribution for the reservoirs. A current is set equal to 1 A at a point in the upper left corner, and as -1 A at the lower right corner and the potential field calculated based on the resistivity of the field at each time step. Figures 3.6 and 3.7 show how the potential difference between the injector and the producer changes with time for the reservoirs shown in Figure 3.3 and 3.4 and Figure 3.8 shows the potential difference time history for the reservoir with no fractures.
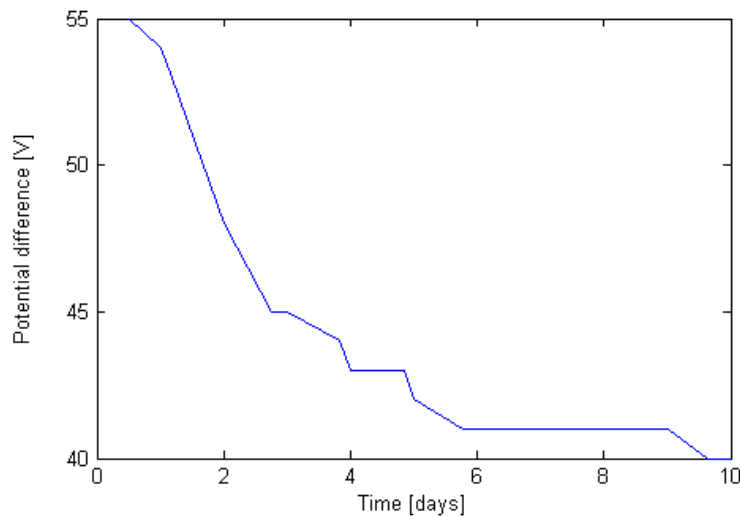

Figure 3.6: Potential difference between injection and production wells for reservoir in Figure 3.3.
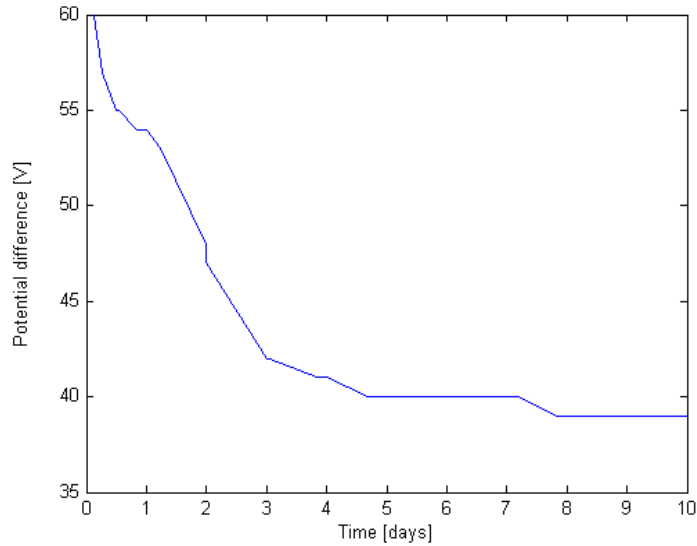
Figure 3.7: Potential difference between injection and production wells for reservoir in Figure 3.4.
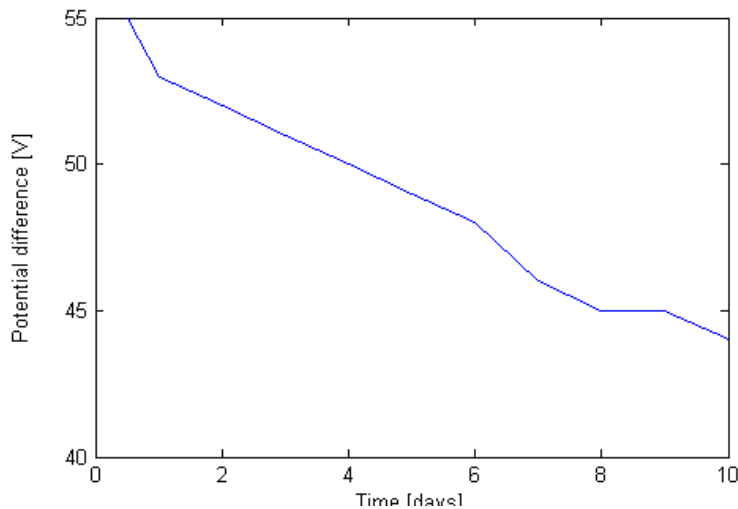
Figure 3.8: Potential difference between injection and production wells for the reservoir with no fractures.

The potential difference in the graph in Figure 3.7 drops faster than the difference in Figure 3.6 because of larger fractures enabling conductive fluid to flow faster through the reservoir. Figure 3.8 shows a much slower decline in potential difference since the reservoir has no fractures. The potential difference after 10 days of injection is 39 V for the larger fractured reservoir, 40 V for the smaller fractured reservoir and 44 V for the reservoir with no fractures. The results also indicate that different fracture properties give different potential difference histories between two wells, and could therefore be used to indicate fracture characteristics.

The results showed how EOS1 module in TOUGH2 was used to solve both tracer flow and electric potential for fracture networks. By using TOUGH2 and the same grid for both simulations, nonrectangular elements could be used making the simulation faster and more efficient. However, since the density and viscosity of the fluid is pressure dependent while the electric conductivity does not depend on the electric potential, the EOS1 module might not give accurate results even though the viscosity does not change drastically within the pressure range used (see Figure 3.1). Therefore, an analytical solution was calculated for a simple flow model, shown in Figure 3.9, to determine whether the EOS1 module in TOUGH2 would give similar results as when EOS9 is used with density and viscosity defined constant.
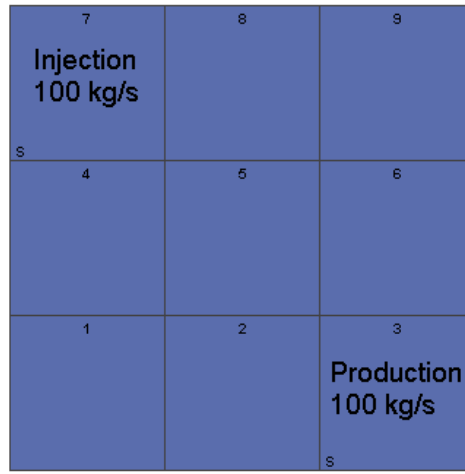

Figure 3.9: A simple flow model with injection and production in opposite corners.

The homogeneous reservoir was modeled with permeability 10^7 md (10^{-8} m^2) and when analytical solution was calculated as well as when EOS9 module of TOUGH2 was used the reservoir was modeled with a constant liquid density of 1000 kg/m^3 and a constant viscosity of 1.7×10^{-4} Pa·s. No-flow boundary conditions were used and 100 kg/s of water was injected in the upper left corner and 100 kg/s produced in the lower right corner. Initial pressure was set to 10^6 Pa. Table 3.3 shows the analytical solution of the pressure which is the same as when EOS9 was used and Table 3.4 shows the pressure calculated using EOS1 module of TOUGH2. The rows of the tables represent the rows of blocks shown in Figure 3.9.

Table 3.3: Pressure [Pa] from analytical solution as well as from using EOS9 module.

1.0013×10^6	1.0004×10^6	1.0000×10^6
1.0004×10^6	1.0000×10^6	9.9958×10^5
1.0000×10^6	9.9958×10^5	9.9873×10^5

Table 3.4: Pressure [Pa] calculated using EOS1 module.

1.0015×10^6	1.0005×10^6	1.0000×10^6
1.0005×10^6	1.0000×10^6	9.9951×10^5
1.0000×10^6	9.9951×10^5	9.9852×10^5

The results when EOS9 module is used are the same as the analytical solution but the results calculated using EOS1 module are a little bit different since the water density and viscosity is pressure-dependent.

Next, the electric field was calculated for a similar 3x3 block matrix using EOS9 and the results compared to the resistivity model previously used for electric field calculations (described in the quarterly report January-March 2011).
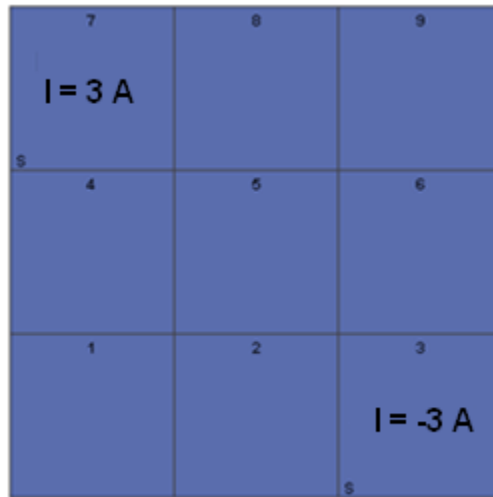

Figure 3.10: Homogeneous electric model with the current set as 3 A in the upper left corner and as -3 A in the lower right corner.

The resistivity was set as 0.1 Ωm and the initial electric potential was set as zero. The electric parameters were scaled as showed in Table 3.2 when EOS9 module was used to solve the electric field. The analytical solution and the solution from the resistivity model were the same as when EOS9 was used. Results are shown in Table 3.5.

Table 3.5: Electric potential calculated using the resistivity model and EOS9 module in TOUGH2 as well as when using the analytical solution.

0.225 V	0.075 V	0 V
0.075 V	0 V	-0.075 V
0 V	-0.075 V	-0.025 V

The matrix shown in Figure 3.11 was studied as well to verify that the scaling used for EOS9 would also work for an inhomogeneous case. The blue blocks have resistivity set as 0.005 Ωm and the green block has the resistivity set as 0.0025 Ωm.
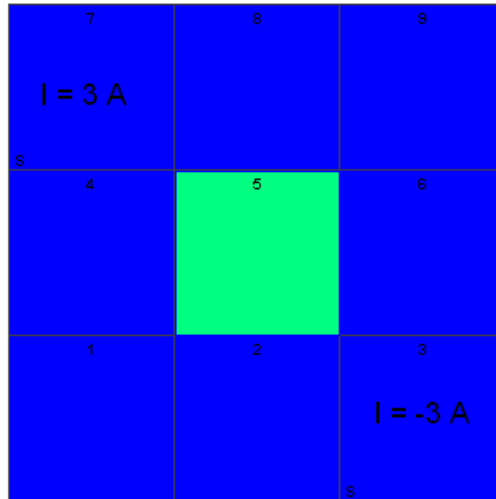
Figure 3.11: Inhomogeneous electric model with the current set as 3 A in the upper left corner and as -3 A in the lower right corner.

The results from using EOS9, see Table 3.6, were the same as the results from the resistivity model and also the same as the analytical solution. Therefore, EOS9 module in TOUGH2 can be used to calculate the electric field accurately by defining the water density and viscosity constant.

Table 3.6: Electric potential calculated using the resistivity model, EOS9 module in TOUGH2 and the analytical solution.

0.0107 V	0.0032 V	0 V
0.0032 V	0 V	-0.0032 V
0 V	-0.0032 V	-0.0107 V

Currently, the model used to calculate the electric potential distribution for the reservoirs shown in Figures 3.3 and 3.4 is being modified so that the accurate electric potential distribution can be calculated for the same reservoirs using EOS9 module in TOUGH2.

3.5 FUTURE WORK

Future work includes looking at more complicated and realistic fracture networks to study further the relationship between fracture networks and the change in potential differences as conductive tracer is injected into the reservoir. Future work also includes implementing self-potential calculations into the model since the change in self-potential affects the measured potential difference and could facilitate fracture characterization. It is of interest as well to study the use of nanotracers and different chemical tracer as well as to explore the influence of injecting varying tracer concentration.

Other future goals are to use tracer concentration simulations and electrical potential calculations from TOUGH2 with inverse modeling to estimate the dimensions and topology of a fracture network. The objective is to develop a method which can be used to find where fractures are located and the character of their distribution.

In inverse modeling the results of actual observations are used to infer the values of the parameters characterizing the system under investigation. In this study, the output parameters would be the potential differences between wells as a function of time and the input parameters would include the dimensions and orientations of the fractures between the wells. The objective function measures the difference between the model calculation (the calculated voltage difference between the wells) and the observed data (measured potential field between actual wells), as illustrated in Figure 3.12, and a minimization algorithm proposes new parameter sets that improve the match iteratively.
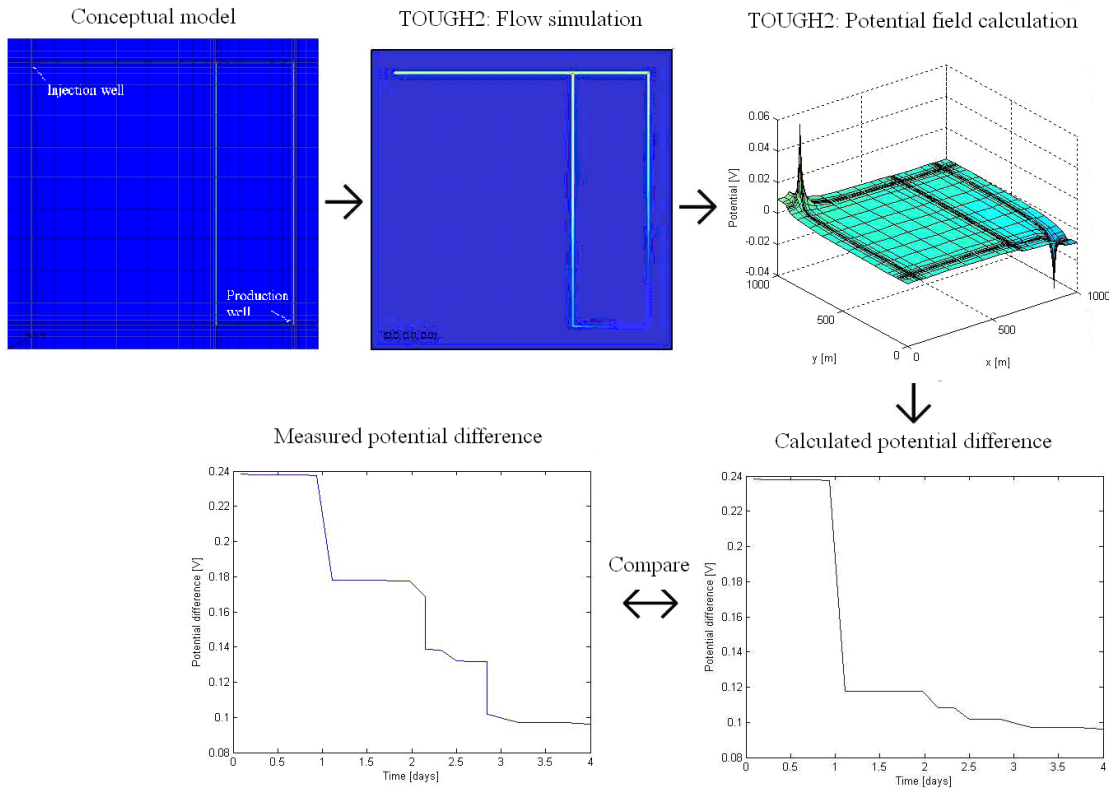

Figure 3.12: The inverse problem; the calculated potential difference is compared to the measured potential difference and the inverse problem solved to characterize fracture patterns.

The possibility of using fewer wells and different well arrangements will be studied to estimate the minimum number of measurement locations necessary to solve the problem.

4. FRACTURE APERTURE DETERMINATION USING THERMAL AND TRACER DATA

This research project is being conducted by Research Associate Carla Kathryn Co and Professor Roland Horne. The overall objective is to develop a methodology to estimate fracture dimensions. Our current focus is on utilizing thermal breakthrough and tracer return data to determine effective fracture apertures.

4.1 SUMMARY

This study aimed to determine the effective aperture of fractures in geothermal reservoir rocks using tracer concentration and thermal breakthrough profiles. A single fracture was used to represent the connectivity between injection and production well pairs. An analytical model derived by Gringarten and Sauty (1975) was used to estimate the fracture aperture from thermal breakthrough time and mean tracer arrival time. Estimated effective fracture aperture values were recalculated and now vary from 2.1 cm to 42.6 cm.

Initially, a literature review was undertaken. Fields included in this study were: Desert Peak, Nevada and Wairakei. New Zealand. Fracture properties were determined from acoustic imaging techniques. Feed zone locations identified through Pressure, Temperature, and Spinner (PTS) data were then correlated to these properties. Results showed that feed zone locations correspond to depths with higher apertures. Fracture density, however, is not relevant to fluid entry zones.

Comparison of cooling rate predictions from three interwell connection models was done this quarter using data from Palinpinon Geothermal Field (Maturgo et al., 2010). These were: single fracture model; porous model with heat loss; and isotropic porous medium model (Bodvarsson, 1972) using ICEBOX. Results for temperature drawdown versus time showed that all three models predict values within 50˚C. This illustrated the viability of using a single effective aperture to characterize producer-injector well connections and predict the thermal effect of different injection scenarios.

4.2 INTRODUCTION

Fracture aperture is an important parameter in geothermal reservoirs. Fracture aperture influences transport and thermal behavior of the reservoir, both in EGS and in conventional hydrothermal systems. An important application is the determination of the degree of interwell connectivity. Of critical importance is the prevention of thermal breakthrough from injection wells to production wells. During the 1980s, several unsuccessful attempts we made to estimate fracture aperture by matching tracer test data. This was because the parameter estimation problem has multiple degrees of freedom, which makes it difficult to separate fracture aperture from other unknown reservoir parameters. To constrain the degrees of freedom, thermal response data could be used. This was proposed in the 1980s, however at the time no data existed that provided both tracer and thermal responses. Now that several EGS and fractured reservoirs have been monitored to provide these data, the possibility now exists to estimate fracture aperture in those fields. In this project, a single fracture model was used to describe the connectivity

of an injection and production well pair. Tracer and thermal data were used to estimate the fracture width for this simplified model.

The objective of the initial work was to determine whether it would be feasible to derive reasonable estimates for the fracture aperture using both thermal and tracer test results. Calculated fracture width estimates were compared to those in the literature to check for consistency. Afterwards, aperture values were reevaluated to account for the actual temperature ratio and to correct previous miscalculations. In addition, studies on fracture characterization using acoustic imaging were reviewed to develop a better understanding of feed zone related fractures. Several attempts to simulate a single fracture between wells were done but were not successful.

Focus this quarter has been on understanding the significance of the derived aperture estimates to predicting reservoir behavior. Cooling predictions from the fracture model were compared to those from two versions of porous models. One is a porous model with heat loss and the other is a tracer-derived model calculated using ICEBOX software (Axelsson, 1995). This was done for the Palinpinon Geothermal field data (Maturgo et al., 2010).

4.3 METHODOLOGY

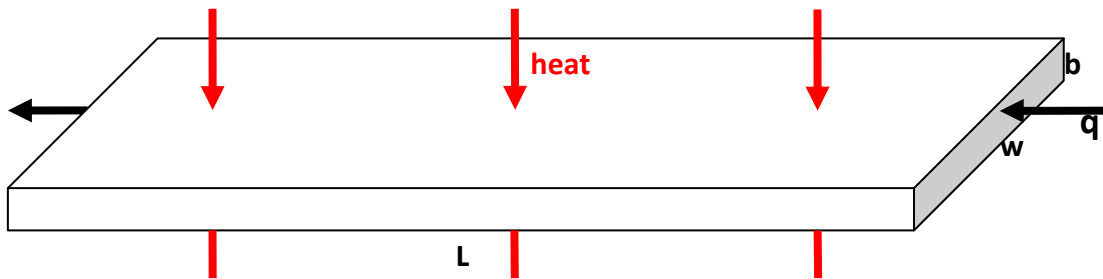### 4.3.1 Analytical Model: Fracture Aperture

Figure 4.1 Model schematic for the Gringarten and Sauty (1975) derivation

Gringarten and Sauty (1975) derived a solution that can be used for unsteady-state one-dimensional heat transfer through a fracture. The solution was similar to that for a porous medium, derived by Lauwerier (1955). The solution assumes a thin, uniform reservoir with an adiabatic boundary. Heat is transferred by conduction from the rock layers and the entering fluid. Since no mixing is assumed, the result is a stream-like channel flow.

Horne (1996) derived the resulting analytical solution for this model as Equation 4.1 where t_c is the tracer front arrival time, t_{th} is the thermal breakthrough time, and b is the fracture aperture. On the left hand side of Equation 4.1 is the relative temperature ratio T_{ratio}. Here, T_o is the original reservoir temperature, T_w is the reservoir temperature at x, and T_{inj} is the injected fluid temperature. Thus, the fracture aperture can be determined using the thermal

and tracer breakthrough data. Knowledge of the fracture aperture can then be used to predict temperature drawdown in producing wells.

$$T_{ratio} = \frac{T_o - T_w}{T_o - T_{inj}} = erfc\left\{ \left[\frac{(\rho_w C_w)^2}{K_r \rho_r C_r} \left(\frac{b}{t_c} \right)^2 (t_{th} - t_c) \right]^{-\frac{1}{2}} \right\} \qquad (4.1)$$

$$b = \left\{ \left(erfc^{-1} \left[\frac{T_o - T_w}{T_o - T_{inj}} \right] \right)^{-2} \frac{t_c^2}{(t_{th} - t_c)} \frac{K_r \rho_r C_r}{(\rho_w C_w)^2} \right\}^{1/2} \qquad (4.2)$$

These are the analytical expressions used to model a single fracture connection between an injector and producer well pair. Equation 4.2 calculates the effective fracture aperture from the thermal arrival time t_{th}; tracer front arrival time t_c; and relative temperature ratio T_{ratio}.

4.3.2 Available field data

Results from tracer tests in EGS and conventional fractured geothermal reservoirs have been reported frequently in the literature. However, thermal breakthrough data are not as widely published. For EGS fields, thermal data were obtained usually from long-term circulation tests, as for example in Hijiori, Matsunaga et al. (2002) and Matsunaga et al. (2005). Historic silica geothermometer data were used from Palinpinon field which is a conventional liquid-dominated reservoir, Maturgo at al. (2010). Matsukawa is a conventional vapor-dominated field, Fukuda at al. (2006). Table 4.1 provides a summary of the field data used in this study. The thermal breakthrough time t_{th} here corresponds to the time it takes to reach a T_{ratio} of 0.5.

Table 4.1: Thermal and tracer breakthrough times from field data.

Field	Injector	Producer	t_c	t_{th}	Source
			days	days	
Hijiori	HDR-1	HDR-2A	1	175	Matsunaga et al. (2002)
	HDR-1	HDR-3	4	266	Matsunaga at al. (2005)
Palinpinon	NJ2RD	NJ5D	15	730[1]	Maturgo at al. (2010)
	SG2RD	NJ3D	28	365	
Matsukawa	M-6	M-8	1.5	146	Fukuda at al. (2006)

---

[1] Assumed that injection in NJ2RD started in 1998 or 1 year before the start of drawdown in NJ5D based on the Palinpinon injection and production history discussed by Bayon and Ogena (2005).

4.3.3 Single Fracture Model: Cooling Rate Prediction

$$T_w = T_o - (T_o - T_{inj})erfc\left\{\left[\frac{(\rho_w C_w)^2}{K_r \rho_r C_r}\left(\frac{qb}{A_{tracer}x}\right)^2\left(t-\left(\frac{\rho_A C_A}{\rho_w C_w}\right)\frac{A_{tracer}x}{q}\right)\right]^{-\frac{1}{2}}\right\} \tag{4.3}$$

$$\rho_A C_A = \phi \rho_w C_w + (1-\phi)\rho_r C_r \tag{4.4}$$

$$A_{tracer} = \phi A_{crosssection} \tag{4.5}$$

$$A_{max} = \frac{q_{total}}{v_{mean}} \tag{4.6}$$

$$q = q_{total}\left(\frac{A_{tracer}}{A_{max}}\right) \tag{4.7}$$

The general equation for temperature versus time as derived by Gringarten and Sauty (1975) is shown in Equation 4.3. Here, x is the distance between the injection well and producer well. Thus, once the aperture b is determined, this equation describes the cooling of producing feedzones due to injection with constant volumetric rate (q) and temperature (T_{inj}). Note that q specified here is not the total injection rate. It is the rate of effective injected volume that goes to a particular producer. This is approximated by getting the ratio of the area derived from tracer analysis to the maximum area based on the total injection rate and the observed mean velocity from tracer data. Equations 4.5 to 4.7 illustrate these in more detail.

4.3.4 Porous Channel with Heat Loss Model: Cooling Rate Prediction

Maturgo et al. (2010) used tracer analysis to determine the effective area (A_{tracer}) for two injector and producer well pairs. These are NJ3D-SG2RD and NJ2RD-NJ5D. Using parameters from the general equation and the effective cross sectional area, thermal velocity without heat loss (v_{th}) can be defined as shown in Equation 4.8. From this definition, Equation 4.3 can be rearranged to get Equation 4.9 which describes the cooling effect of injection for a porous connection model. As explained in the previous section, q is the effective volumetric injection rate.

$$v_{th} = \frac{q}{A_{tracer}}\frac{\rho_w C_w}{\rho_A C_A} = v_w\phi \tag{4.8}$$

$$T_w = T_o - (T_o - T_{inj})erfc\left\{\left[\frac{(\rho_A C_A)^2}{K_r \rho_r C_r}\frac{v_{th}^2 b^2}{x^2}\left(t-\frac{x}{v_{th}}\right)\right]^{-\frac{1}{2}}\right\} \tag{4.9}$$

4.4 PRELIMINARY CALCULATIONS AND RESULTS

4.4.1 Fracture Aperture

As described in the previous section, fracture aperture can be estimated directly from the thermal and tracer breakthrough time. Assumptions for the values of the other parameters are listed in Table 4.2. These were the values assigned to these properties in the estimation of fracture aperture. Actual temperature ratios for the injector-producer pairs derived from long term circulation test results are shown in Table 4.3. Estimated fracture aperture values are given in the same table.

To determine the relative temperature for M-6 and M-8 in Matsukawa, a 60$^{\text{o}}$C injection temperature was assumed. Estimates of effective fracture aperture b vary from 2.1 cm to 42.6 cm. Though the HDR-1 and HDR-2A well pair in Hijiori exhibited the shortest mean tracer arrival time, it had the lowest calculated effective aperture value because of the long thermal breakthrough time. This observation demonstrates the value of using both tracer and thermal results to constrain the effective aperture. Using this analytical solution also provides an alternative method to characterize the flow path between wells.

Results from finite element heat and mass transfer modeling (FEHM) of the Hijiori field demonstrates fracture aperture values of about 2 mm (Tenma et al., 2005). This is significantly lower than the calculated aperture values. Further investigation of results from aperture estimates from numerical modeling will be undertaken. However, effective fracture aperture derived from acoustic imaging logs show a range of values consistent with those calculated. The next section will describe these studies in detail.

Table 4.2: Assumptions used in calculations.

Rock thermal conductivity	K_r	2	W/m-C
Rock density	ρ_r	2200	kg/m^3
Water density	ρ_w	900	kg/m^3
Rock heat capacity	C_r	0.712	kJ/kg-C
Water heat capacity	C_w	4.342	kJ/kg-C

Table 4.3: Relative temperature ratios and calculated fracture aperture from thermal and tracer breakthrough times.

Field	Injector	Producer	T_{ratio}	Calculated b cm
	HDR-1	HDR-2A	0.46	2.1
Hijiori	HDR-1	HDR-3	0.14	6.9
	NJ2RD	NJ5D	0.17	15.7
Palinpinon	SG2RD	NJ3D	0.07	42.6
Matsukawa	M-6	M-8	0.29[2]	3.5

---

[2] Assumed an injection temperature of 60$^{\text{o}}$C

4.4.2 Cooling Predictions

Comparison of cooling predictions was the most convenient way of relating the various producer-injector well connection models to each other. We wanted to investigate if they would give similar temperature drawdown profiles. Assumptions used for cooling rate calculations are shown in Table 4.4. Area values used to determine the effective injection rate going to the producer are in Table 4.5. These values were used by Maturgo et al. (2010) to predict the temperature drawdown due to injection at a constant rate (q_{total}) and temperature (T_{inj}). Palinpinon data was chosen because it had detailed cooling rate calculations available in literature. This also served as an additional verification of the validity of our models and the results of our calculations.

Table 4.4: Parameters used for cooling rate predictions

Field	Injector	Producer	q_{total} m^3/s	T_o C	T_{inj} C	L m
Palinpinon	NJ2RD	NJ5D	0.178	265	160	1500
	SG2RD	NJ3D	0.117	265	160	1500

Table 4.5: Effective injection rate calculation

Field	Injector	Producer	A_{max} m^2	A_{tracer} m^2	q m^3/s
Palinpinon	NJ2RD	NJ5D	217.5	50.7	0.041
	SG2RD	NJ3D	175.8	39.7	0.027

Cooling rate or temperature drawdown predictions from three models were compared. First was the single fracture model as described in Equation 4.3. Next was the porous model with heat loss using Equation 4.9. The third one was the isotropic porous medium model derived by Bodvarsson (1972) calculated using the ICEBOX software (Axelsson, 1995 and Axelsson, 2005). As described in the previous section, calculation of temperature drawdown for the first two models was straightforward. On the other hand, values for the third model were just lifted from the same paper where data for aperture calculations were obtained (Maturgo et al., 2010).

Figure 4.2 shows the results for NJ2RD-NJ5D while Figure 4.3 illustrates the forecast for NJ3D-SG2RD. Time in the x-axis is measured from the start of injection. For NJ2RD-NJ5D, the fracture model gives a prediction very similar to the one using ICEBOX. However, the porous model for this well pair presents a more pessimistic temperature forecast. On the other hand, both the porous model and fracture model agree on a lower stabilized temperature than the ICEBOX model prediction for NJ3D-SG2RD as seen in Figure 4.3. It is still unclear why the three models behaved differently for these two scenarios. Still, it is good that all three models agree within a range of 50 ˚C. This proves

that the effective single fracture aperture model is a viable one since it can be used to predict injection effects. Further investigation using numerical modeling as well as data from other geothermal fields will have to be made.
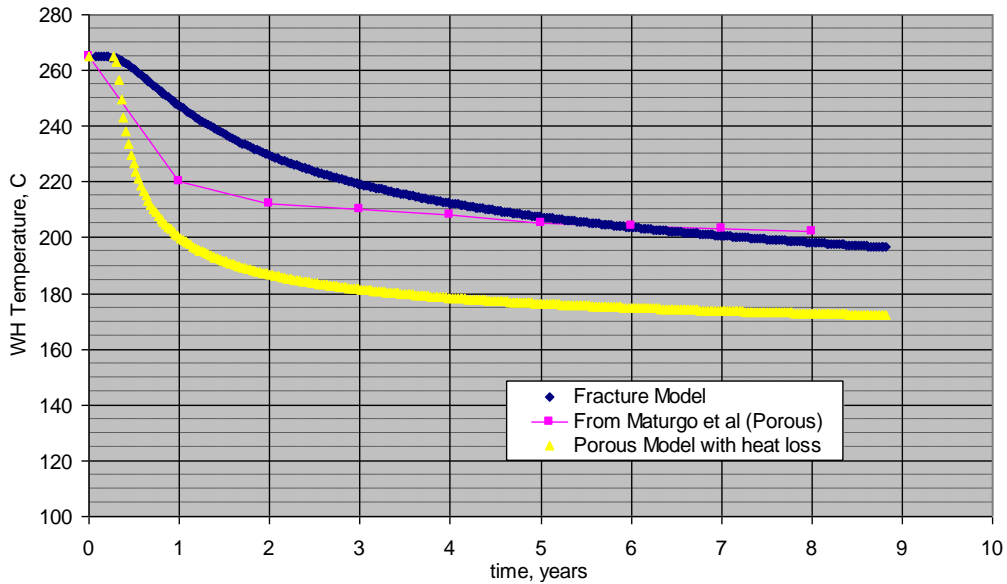

Figure 4.2 Comparison of cooling predictions for NJ2RD-NJ5D from different models: (1) fracture model; (2) porous model with heat loss; (3) ICEBOX (Maturgo et al.,2010).
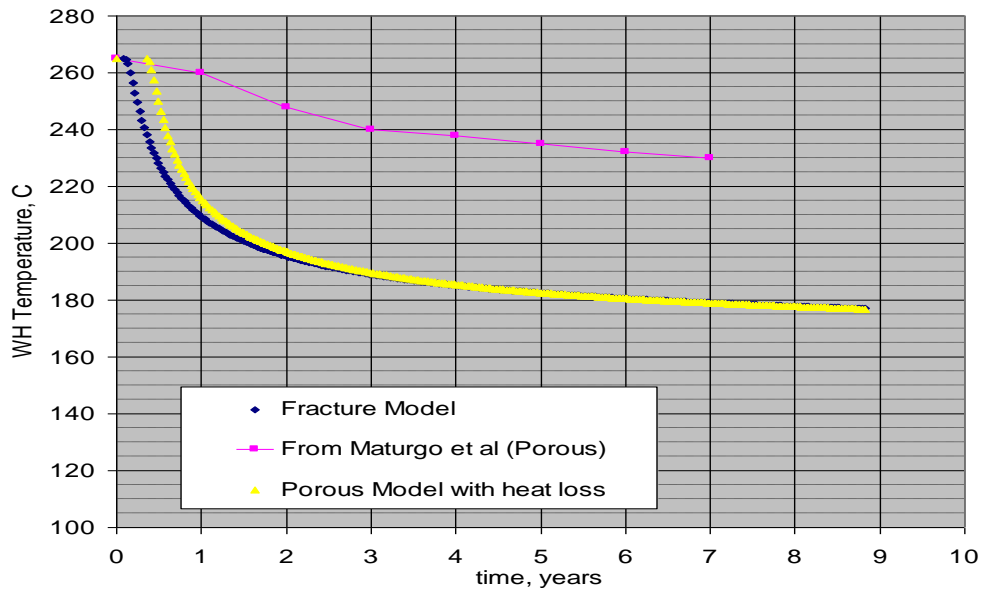

Figure 4.3 Comparison of cooling predictions for NJ3D-SG2RD from different models: (1) fracture model; (2) porous model with heat loss; (3) ICEBOX (Maturgo et.al, 2010).

4.5 REVIEW OF RELATED LITERATURE

4.5.1 Acoustic Imaging

Characterization of fluid flow in fractures is an important area of study in geothermal reservoir engineering. Overall permeability in these reservoirs is fault-dominated (Massart, 2010). Relevant fracture parameters to fluid flow are: orientation, aperture, extension, and density. These parameters influence transport and thermal behavior of the reservoir, both in enhanced geothermal systems (EGS) and in conventional hydrothermal systems. Recent advances in borehole imaging technology have made it possible to measure fracture properties with greater accuracy.

For the Wairakei geothermal field, McLean and McNamara (2011) used a high temperature acoustic formation imaging tool (AFIT) to collect fracture data. Confidence, azimuth, and amplitude filters were applied to the data prior to analysis. A borehole televiewer (BHTV) similar to AFIT and UBI was also used in the Desert Peak EGS project. In addition, formation microscanner (FMS) image logs were utilized (Devatzes, 2009).

Published fracture data from various geothermal fields were collected and analyzed. Data sets examined for this study are fracture aperture and density. These were then compared to locations of feed zones to determine their correlation with fluid flow properties.

Fracture data from the various geothermal fields show consistent correspondence between fracture apertures and feed zone locations for most of the data points. In Wairakei, fracture apertures for the feed zones range from around 10 to 60 centimeters in wells WK-404, WK-318, and WK-407. A similar trend can be observed from the Desert Peak data. Data for well 27-15 had aperture values from 3 to 10 cm at fluid entry zones. Figures 4.4 to 4.7 show the feed zone locations, PTS data, and fracture apertures for various wells in Wairakei and Desert Peak.

There are two possible explanations for this observation. Using a parallel-plate model, fracture permeability is proportional to b^3, where b is the fracture aperture (Jourde, 2002). Fluid entry, associated to fractures in geothermal reservoirs, occurs at depths with high permeability. Therefore, feed zone locations will be at depths with high apertures. Another rationale is the power-law scaling between joint length and width described by Scholz (2010). Scholz argued that for opening mode in rocks, fracture toughness scales linearly with $\sqrt{L}$ and b scales linearly with L, where L is the length. Therefore, a larger fracture width will correspond to a longer fracture which implies a farther reach for the fluid source.

On the other hand, there appears to be no correlation between fracture density and feed zone depths. Massart et al. (1999) analyzed new data sets from natural faults and extension fractures and validated that it follows power-law scaling in multiple-observational scales. Results from their study show that the power-law scaling applies across six ranges of scale within reasonable uncertainty limits. Zones with higher fracture

aperture values will have smaller fracture density. Based on this, regions with higher apertures will have lower fracture density values. Hence, fluid entry points should have lower fracture densities. However, this was not consistently observed in all the data. The lack of inverse correspondence between fracture density and feed zone location could be due to the binning of data. Tool measurement uncertainties could also cause deviations. Moreover, there is inherent error associated with the inverse scaling of fracture density and aperture.
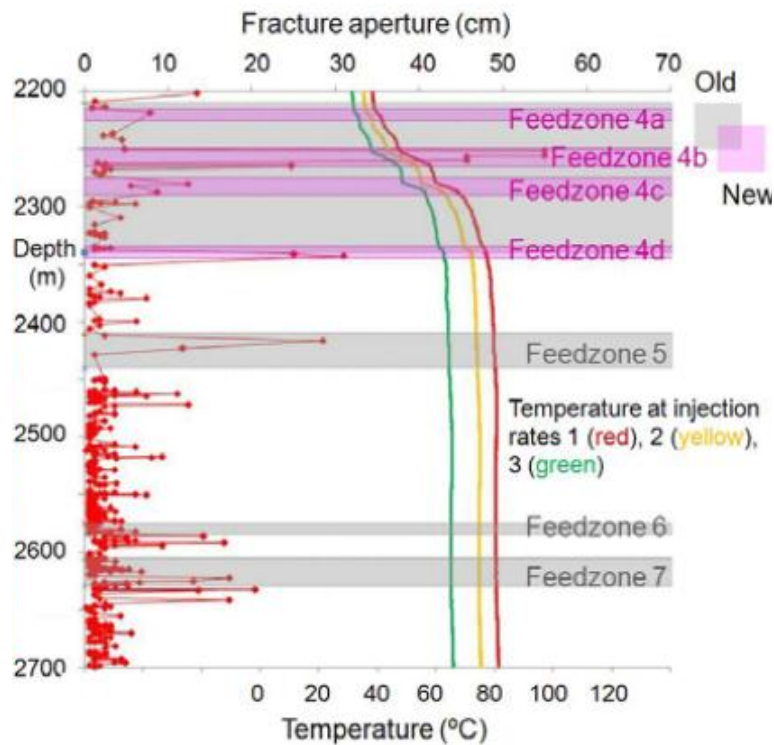

Figure 4.4 Fracture aperture (red) and temperature versus depth for well WK-404 in the Wairakei Geothermal Field, from McLean and McNamara, 2011).
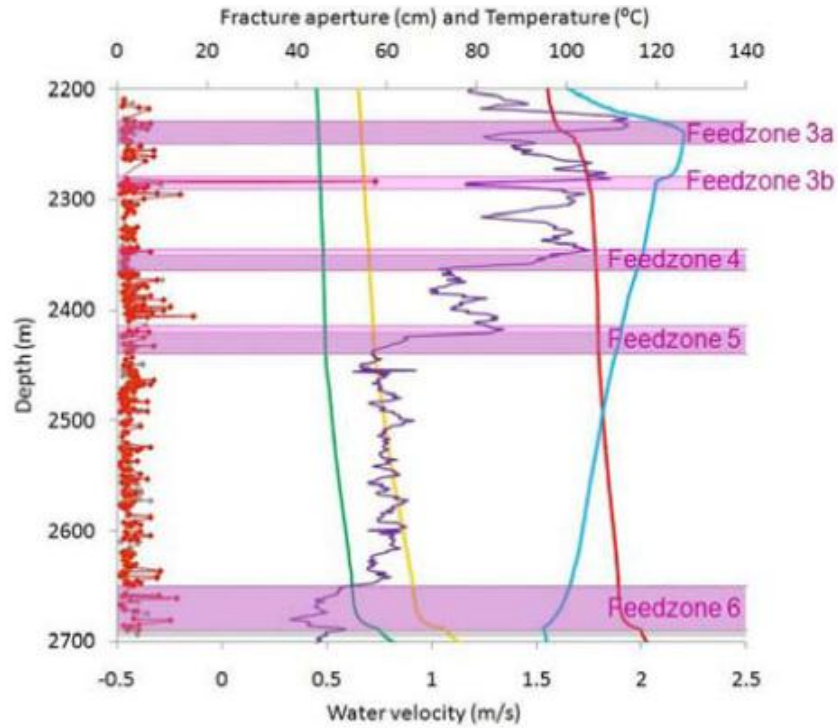
Figure 4.5 Fracture aperture (red), temperature, and spinner velocity (blue) versus depth log for well WK-317 in the Wairakei Geothermal Field (from McLean and McNamara, 2011).
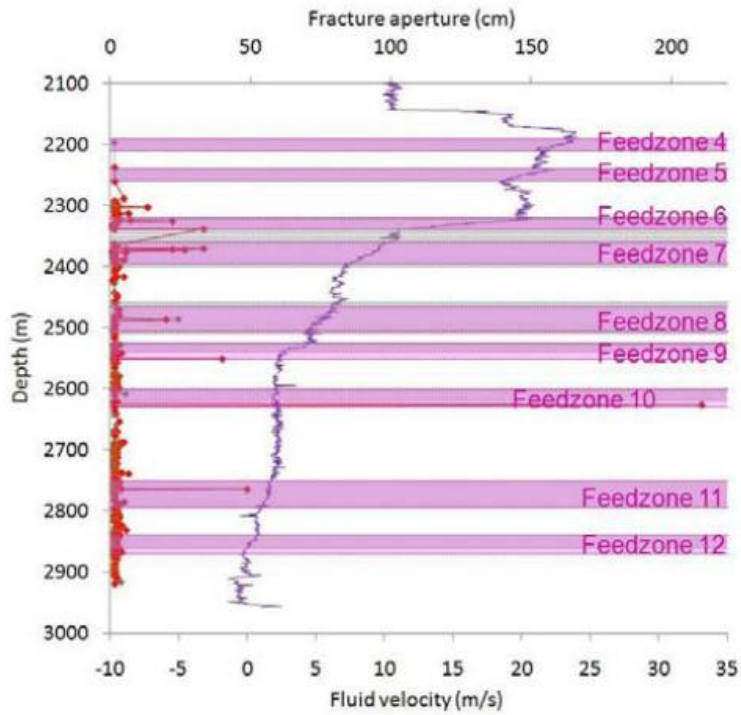

Figure 4.6 Aperture (red) and spinner velocity (blue) versus depth log for well WK-407 in the Wairakei Geothermal Field (from McLean and McNamara, 2011).
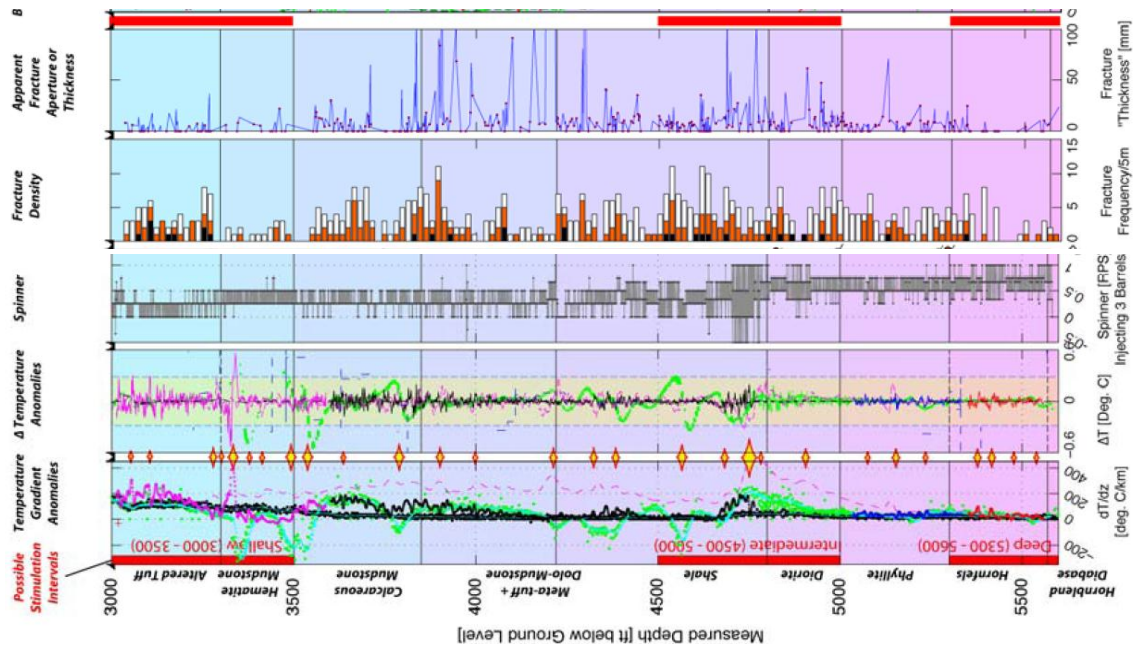
52

Figure 4.7 Well Log data for well 27-15 in the Desert Peak Geothermal Field, Nevada. Yellow diamonds indicate feed zones derived from temperature anomalies and spinner velocities (Devatzes, 2009)

4.6 FUTURE WORK

Further review of recently published data will be undertaken. Use of pressure transient analysis for fracture characterization will also be explored. To avoid instability problems during numerical simulations in TOUGH2, Feflow will be used instead. This program is does not have phase change modeling capability. However, it would suffice for this particular modeling application because the fluid remains single phase. Moreover, the program is more stable especially in handling tracer modeling. It is anticipated that simulated results from the analytical model of the idealized fracture connection can be compared to an equivalent numerical model. Comparison of temperature will be done at various locations and time steps. Additional configurations of fracture connectivity will be simulated using the same software.

5. REFERENCES

Bayon, F.E.B. and Ogena, M.S.: "Handling the Problem of Rapid Reinjection Returns in

Palinpinon-I and Tongonan, Philippines," *Proceedings* World Geothermal Congress. 2005.

Devatzes, N.C. and Hickman, S.H.: "Fractures, stress, and fluid flow prior to stimulation of well 27-15, Desert Peak, Nevada, EGS project," *Proceedings* 34th workshop on Geothermal Reservoir Engineering, Stanford University. 2009.

Devatzes, N.C. and Hickman, S.H.: "In-situ stress and fracture characterization for planning of an EGS stimulation in the Desert Peak Geothermal Field, Nevada," *Proceedings* 35th workshop on Geothermal Reservoir Engineering, Stanford University. 2010.

Fukuda, D., Akatsuka, T., and Sarudate, M: "Characterization of inter-well connectivity using alcohol tracer and steam geochemistry in the Matsukawa vapor-dominated geothermal field, Northeast Japan," *GRC Transactions*. 2006, 797-801.

Gringarten, A.C. and Sauty, J. P.: "A theoretical study of heat extraction from aquifers with uniform regional flow," *Journal of Geophysical Research*. 1975, 4956-122.

Horne, R.N.: "Reservoir Engineering of Reinjection," Course Notes. Stanford University, 1996.

Jourde, H. et.al.: "Computing permeability of fault zones in eolian sandstone from outcrop measurements," *American Association of Petroleum Geologists Bulletin*. 2002.

Marrett, R. et.al.: "Extent of power-law scaling for natural fractures in rock," *Geology*. 1999.

Massart, B. et.al.: "Fracture characterization and stochastic modeling of the granitic basement in the HDR Soultz Project (France)," *Proceedings,* World Geothermal Congress. 2010.

Matsunaga, I., Yanagisawa, N., Sugita, H., Tao, H.: "Reservoir monitoring by tracer testing during a long term circulation test at the Hijiori HDR site," *Proceedings*, Twenty-Seventh Workshop on Geothermal Reservoir Engineering, Stanford University. 2002.

Matsunaga, I., Yanagisawa, N., Sugita, H., Tao, H.: "Tracer tests for evaluation of flow in a multi-well and dual fracture system at the Hijiori HDR test site," *Proceedings*, World Geothermal Congress. 2005.

Maturgo, O.O., Sanchez, D. R., and Barroca, G.B.: "Tracer test using naphthalene disulfonates in Southern Negros Geothermal Production Field, Philippines," *Proceedings*, World Geothermal Congress. 2010.

McLean, K. and McNamara, D.: "Fractures interpreted from acoustic formation imaging technology: correlation to permeability," *Proceedings,* 36th workshop on Geothermal Reservoir Engineering, Stanford University. 2011.

Pruess, K. and Bodvarsson, G. S.: "Thermal effects of reinjection in geothermal reservoirs with major vertical fractures," *Journal of Petroleum Technology*. 1984, 1567-1578.

Scholz, C.H.: "A note on the scaling relations for opening mode fractures in rock," *Journal of Structural Geology*. 2010.

Tenma, N., Yamaguchi, T., and Zyvoloski, G.: Variation of the characteristics of the shallow reservoir at the Hijiori test site between 90-days circulation test and long-term circulation test using FEHM code." *Proceedings*, World Geothermal Congress. 2005.

Holder, D.S.: Electrical Impedance Tomography: Methods, History and Applications, IOP, UK (2004).

Pritchett, J.W.: Finding Hidden Geothermal Resources in the Basin and Range Using Electrical Survey Techniques. A Computational Feasibility Study, report INEEL/EXT-04-02539 (2004).

Singha, K. and Gorelick, S.M. Saline Tracer Visualized with Three-dimensional Electrical Resistivity Tomography: Field-scale Spatial Moment Analysis. *Water Resources Research*, **41** (2005), W05023.

Slater, L., Binley, A.M., Daily, W. and Johnson, R. Cross-hole Electrical Imaging of a Controlled Saline Tracer Injection. *Journal of Applied Geophysics*, **44**, (2000), 85-102.

Stacey, R.W., Li, K. and Horne, R.N.: Electrical Impedance Tomography (EIT) Method for Saturation Determination, *Proceedings*, 31st Workshop on Geothermal Reservoir Engineering, Stanford University, Stanford, CA (2006).

Ucok, H., Ershaghi, I. and Olhoeft, G.R.: Electrical Resistivity of Geothermal Brines, *Journal of Petroleum Technology*, **32**, (1980), 717-727.

Wang, P. and Horne, R.N.: Integrating Resistivity Data with Production Data for Improved Reservoir Modeling, SPE 59425, SPE Asia Pacific Conference, Yokohama, Japan (2000).

Alaskar, M., Ames, M., Horne, R.N., Li, K., Connor, S. and Cui, Y.: "In-situ Multifunction Nanosensors for Fractured Reservoir Characterization," GRC Annual Meeting, Sacramento, USA, vol. 34 (2010).

Alaskar, M., Ames, M., Horne, R.N., Li, K., Connor, S. and Cui, Y.: "Smart Nanosensors for In-situ Temperature Measurement in fractured geothermal reservoirs," GRC Annual Meeting, San Diego, USA, (2011).

Chen, Chih-Ying: Liquid-gas Relative Permeability in Fractures: Effects of Flow Structures, Phase Transformation and Surface Roughness, PhD thesis, Stanford University, Stanford, California (2005).

Diomampo, G.P.: Relative Permeability through Fractures, MS thesis, Stanford University, Stanford, California (2001).

Den Iseger, P., Numerical transform inversion using Gaussian quadrature. *Probability in the Engineering and Informational Sciences*, **20(01)**, (2005), 1–44.

Kocabas, I., Designing Thermal and Tracer Injection Backflow Tests, *World Geothermal Congress,* (2010).

Lauwerier, H. A., The transport of heat in an oil layer caused by the injection of hot fluid. *Applied Scientific Research*, **5(2)**, (1955) 145-150.

Stehfest, H., Numerical inversion of Laplace transforms. *Communications of the ACM*, **13(1)**, (1970), 47-49.

Valkó, P. P., and J. Abate, Numerical inversion of 2-D Laplace transforms applied to fractional diffusion equations, *Applied numerical mathematics*, **53(1)**, (2005), 73–88.